

Development of an Efficient Meso-scale Multi-phase Flow Solver in Nuclear Applications

Nuclear Energy Advanced Modeling & Simulation

Taehun Lee

CCNY, City University of New York

In collaboration with:

Argonne National Laboratory

Tansel Selekler, Federal POC

David Pointer, Technical POC

FINAL REPORT

Project Title: Development of an Efficient Meso-scale Multi-phase Flow Solver in Nuclear Applications

Covering Period: October 1, 2011 through September 30, 2015

Date of Report: October 20, 2015

Recipient: City College of New York
160th Convent Ave.
New York, NY 10031

Award Number: NEUP 11-3006

PI: Taehun Lee, (212) 650-6122, thlee@ccny.cuny.edu

Co-PIs: Kent Wardle, kwardle@anl.gov
Masahiro Kawaji, kawaji@me.ccny.cuny.edu
Sanjoy Banerjee, sbacrs@gmail.com

Project Abstract: The proposed research aims at formulating a predictive high-order Lattice Boltzmann Equation for multi-phase flows relevant to nuclear energy related application - namely, saturated and sub-cooled boiling in reactors, and liquid-liquid mixing and extraction for fuel cycle separation. An efficient flow solver will be developed based on the Finite Element based Lattice Boltzmann Method (FE-LBM), accounting for phase-change heat transfer and capable of treating multiple phases over length scales from the submicron to the meter. A thermal LBM will be developed in order to handle adjustable Prandtl number, arbitrary specific heat ratio, a wide range of temperature variations, better numerical stability during liquid-vapor phase change, and full thermo-hydrodynamic consistency. Two-phase FE-LBM will be extended to liquid-liquid-gas multi-phase flows for application to high-fidelity simulations building up from the meso-scale up to the equipment sub-component scale. While several relevant applications exist, the initial applications for demonstration of the efficient methods to be developed as part of this project include numerical investigations of Critical Heat Flux (CHF) phenomena in nuclear reactor fuel bundles, and liquid-liquid mixing and interfacial area generation for liquid-liquid separations. In addition, targeted experiments will be conducted for validation of this advanced multi-phase model.

Summary of Effort Performed and Accomplishments Achieved

The Research Foundation at City College of New York has received the funding from DOE NEUP program in mid-January 2012.

Table 1 shows three milestones and deliverables originally proposed for the first three years.

Table 1: Milestones and Deliverables

	Milestones	Deliverables
Year 1	<ul style="list-style-type: none"> - Develop an isothermal two-phase FE-LBM with improved stability and parallel performance - Investigate liquid-liquid fuel separation process - Test DNS/Advanced LES model 	<ul style="list-style-type: none"> - Efficient isothermal, two-phase FE-LBM code for massively parallel architecture - Meso-scale LB theory and algorithm liquid-liquid mixing and extraction - DNS/LES capability for simple flows
Year 2	<ul style="list-style-type: none"> - Complete formulation of thermal and multi-component LBM - Investigate nucleate and flow boiling process - Complete computational validation - Incorporate Advanced LES model 	<ul style="list-style-type: none"> - Meso-scale LB theory and algorithm for boiling and liquid film dryout - An Interim Report containing new findings and validation results - DNS/LES capability for two-phase flows
Year 3	<ul style="list-style-type: none"> - Complete experimental validation of saturated and sub-cooled flow boiling - Complete experimental validation of liquid-liquid-gas mixing and extraction 	<ul style="list-style-type: none"> - Efficient <i>thermal, multi-phase</i> FE-LBM code for massively parallel architecture

New milestones and deliverables were proposed for the fourth year as presented in Table 2.

Table 2: New Milestones and Deliverables

	Milestones	Deliverables
Year 4	<ul style="list-style-type: none"> - Complete computational validation of FE-LBM for various bubbly flows at high Reynolds number - Complete comparison of FE-LBM with existing two-phase flow codes such as OpenFOAM and Gerris 	<ul style="list-style-type: none"> - Efficient and novel Adaptive Mesh Refinement (AMR) Lattice Boltzmann Method (LBM) for solving two-phase flows - A new Spectral Element Discontinuous Galerkin Lattice Boltzmann Method code (also known as NEK-LBM) for two-phase flows - A Final Report containing new findings and validation results

A detailed description of the efforts applied to and the results obtained toward achievement of objectives of the work is presented in the following. Uncompleted objectives are underlined.

YEAR 1:

- 1) The original two-phase FE-LBM code was based on the pressure-momentum formulation of the lattice Boltzmann equation (LBE) supplemented by the Cahn-Hilliard equation for interface tracking. The momentum formulation requires relatively large interface thickness to resolve sharp phase-interface region, typically 4-5 finite elements for stability, in which

water and its own vapor are separated by van der Waals type force [1]. We have proposed a new approach based on the pressure-velocity formulation of LBE, which could substantially improve the stability of FE-LBM while decreases the minimum required interface thickness down to 2 elements accelerating convergence toward sharp interface limit. Later we have found out, however, this formulation required more work for consistency. This effort has been made for another 3 years to complete and, therefore no publication or presentation was made with the new pressure-velocity formulation in YEAR 1.

- 2) An efficient iteration scheme on parallel machines is incorporated into the FE-LBM code, which relies on the lumped-mass solution of the advection of particle distribution functions and intermolecular forces as the initial guess of the iterative solver. This improved the solution time by a factor of 2 or 3 compared with the popular preconditioned Conjugate Gradient method. The code has been tested on Cray XT machine located in CUNY HPC center.
- 3) Based on the pressure-momentum formulation, free-surface flows inside a rotating concentric cylinder was studied, which has a relevance in centrifugal contactor applications. Due to the stability reason as described above, the Reynolds number of the free surface flows was $O(1,000)$, which is an order of magnitude smaller than in the actual contactor applications, but the agreement with the existing benchmark experiments was acceptable. This effort was published in a journal paper [2]. In addition to the stability issue, we have found out that the Cahn-Hilliard type equation cannot conserve mass when drops or bubbles become smaller than the certain critical radius [3-5]. We have recently proposed a model that conserves the mass of small drops and bubbles in YEAR 4 [6].
- 4) Vremans LES model was incorporated into the FE-LBM code.

YEAR 2:

- 1) There are two major directions to develop thermal LBM; One based on a fully compressible formulation with the proper *equation of state* (EOS) that automatically deals with phase separation and change due to pressure and temperature variations, and the other based on a *modified incompressible formulation* with modeled mass flow rate due to phase change occurring at *sharp phase interface*. Although EOS based formulation is general and applicable to a variety of flow situations, it lacks numerical stability as the density ratio increases when the system deviates from the critical point. Since our goal was to achieve simulation capability of flow boiling at higher Reynolds number, we have decided to develop the modified incompressible formulation. This objective was not accomplished in YEAR 2 due to the difficulties involving the definition of mass flow rate at the phase interface in Cahn-Hilliard fluids. In YEAR 4, we were able to develop a model that conserves the mass.
- 2) Vremans LES model was tested for two-phase free surface flows inside a rotating concentric cylinder at $Re = 40,000$. LES of free surface flows was not completed due to the mass conservation issue of the Cahn-Hilliard based FE-LBM. When a free surface undergoes breakup process, small droplets tend to disappear into the gas phase in order to minimize the Cahn-Hilliard free energy. It is expected that the new hybrid model developed in YEAR 4 will have the capability to simulate high Reynolds number free surface flow simulations inside a concentric cylinder. This effort will continue even after the present project is over.

YEAR 3:

- 1) Subcooled flow boiling experiments have been conducted using water at atmospheric pressure in a rectangular flow channel. These experiments are conducted to obtain high-resolution data for validation of 3-D Interface Tracking Models (ITMs) and CFD models which can predict subcooled flow boiling phenomena in fuel assemblies of Pressurized Water Reactors. The data needed for model validation include turbulent liquid flow characteristics, vapor bubble nucleation, growth and departure data, and wall temperature response during subcooled flow boiling [7].
- 2) Development of thermal two-phase LBM was completed, while its implementation in FE-LBM has not been completed. We have recently developed a hybrid sharp-interface thermal and diffuse-interface hydrodynamic LBM model, which accurately models mass flow rate due to latent heat across the phase interface [8]. Its implementation in the framework of Galerkin finite element method requires further research.

YEAR 4:

- 1) The new pressure-velocity formulation for FE-LBM has been completed and applied to bubbly flows at high Reynolds numbers ($Re \sim O(10,000)$) in both 2D and 3D. A new conservative phase-field model was hybridized with the Cahn-Hilliard model delivering an excellent mass conservation property [4,9].
- 2) Dynamic Adaptive Mesh Refinement (AMR) technique was developed on a uniform rectangular mesh. This technique utilizes the fact that LBM becomes most accurate at the highest level of refinement and reduces the Lax-Wendroff type 2nd-order accurate scheme on the lower levels of refinement [10-12]. The AMR technique has been applied for 2D single-phase and two-phase flows. It has not been extended to FE-LBM code yet.
- 3) Comparison with OpenFOAM has not been accomplished due to lack of resources.
- 4) Spectral-Element Discontinuous Galerkin LBM (SEDG-LBM), also known as Nek-LBM [13,14] was extended to two-phase flows, in which the formulation and discretization of the intermolecular forcing term or surface tension term are of utmost importance for both stability and accuracy. We have recently developed a novel Strang-Splitting for the complex intermolecular forcing terms in LBM. This splitting can successfully eliminate the parasitic currents that are unavoidable in almost all two-phase flow codes and was shown to substantially enhance the stability of the two-phase LBM code. We are currently working on single-distribution function Nek-LBM and two-distribution Nek-LBM for compressible and incompressible two-phase flow simulations, respectively [15]. Nek-LBM shares the same code structure as the NEAMS thermal-hydraulics code NEK5000 and any successful formulations developed for Nek-LBM could potentially be utilized in Nek5000.

List of Peer-Reviewed Journal Publications

([†]graduate advisee, [‡]postdoctoral advisee)

1. A. Fakhari[†] and T. Lee, "Multiple-Relaxation-Time Lattice Boltzmann Method for Immiscible Fluids at High Reynolds Numbers," *Physical Review E* **87**: 023304 (2013)
2. K.E. Wardle and T. Lee, "Finite Element Lattice Boltzmann Simulations of Free Surface Flow in a Concentric Cylinder," *Computers & Mathematics with Applications* **65**: 230–238 (2013)
3. L. Zheng[‡], T. Lee, Z. Guo, and D. Rumschitzki, "Shrinkage of Bubbles/Drops in the Lattice Boltzmann Equation Method for Nonideal Gases," *Physical Review E* **89**: 033302 (2014)
4. M.C. Geier, A. Fakhari[†], and T. Lee, "Conservative Phase-field Lattice Boltzmann Equation for Interface Tracking," *Physical Review E* **91**: 063309 (2015)
5. L. Baroudi[†], M. Kawaji, and T. Lee, "Effects of Initial Conditions on the Simulation of Inertial Coalescence of Two Drops," *Computers & Mathematics with Applications* **67**: 282–289 (2014)
6. L. Baroudi[†], S.R. Nagel, J.F. Morris, and T. Lee, "Dynamics of Viscous Coalescing Droplets in a Saturated Vapor Phase," *Physics of Fluids* **27**: 121702 (2015)
7. R. Samaroo[†], N. Kaur[†], K. Itoh, T. Lee, S. Banerjee, and M. Kawaji, "Turbulent Flow Characteristics in an Annulus under Air Bubble Injection and Subcooled Flow Boiling Conditions," *Nuclear Engineering & Design* **268**: 203–214 (2014)
8. M. Mohammadi-Shad, M. Kawaji, and T. Lee, "Pressure Evolution Lattice Boltzmann Modeling of Liquid-vapor Thermal Phase Change," submitted to *Physical Review E* (2016)
9. L. Baroudi[†] and T. Lee, "A Hybrid Conservative Phase Field and Cahn-Hilliard Model for Two-phase Lattice Boltzmann Method for High Reynolds Number," submitted to *Journal of Computational Physics* (2016)
10. A. Fakhari[†] and T. Lee, "A Finite Difference Lattice Boltzmann Model with a Block-structured Adaptive Mesh Refinement Technique," *Physical Review E* **89**: 033310 (2014)
11. A. Fakhari[†] and T. Lee, "Numerics of the Lattice Boltzmann Method on Nonuniform Grids: Standard LBM and Finite-difference LBM," *Computers & Fluids* **107**: 205–213 (2015)
12. A. Fakhari[†], M.C. Geier, and T. Lee, "A Mass-conserving Lattice Boltzmann Method with Dynamic Grid Refinement for Immiscible Two-phase Flows," submitted to *Journal of Computational Physics* (2015)
13. K.C. Uga[†], M. Min, T. Lee, and P.F. Fischer, "Lattice Boltzmann Simulations of Flow Past Two Cylinders in Tandem using Spectral-Element Discontinuous Galerkin Approach with Exponential Time Integrator," *Computers & Mathematics with Applications* **65**: 239–251 (2013)
14. S. Patel[†], M. Min, K.C. Uga[†], and T. Lee, "Spectral-Element Discontinuous Galerkin Lattice Boltzmann Method for Simulating Natural Convection Heat Transfer in a Horizontal Concentric Annulus," *Computers & Fluids* **95**: 197–209 (2014)
15. S. Patel[†] and T. Lee, "A New Splitting Scheme to the Discrete Boltzmann Equation for Non-ideal Gases on Unstructured Grids," submitted to *Journal of Computational Physics* (2016)

Results Obtained Toward Achievement of Objectives

1. Development of an Efficient Isothermal FE-LBM for Two-Phase Flow

LBM is a mesoscale approach, which can accommodate coarse-grained, molecular-level information into the macroscopic description of complex interfacial phenomena. This is achieved by introducing a phase field function into a single-phase lattice Boltzmann formulation to distinguish between phases (i.e. liquid/vapor, liquid/liquid, or liquid/liquid/gas), together with a phenomenological free energy functional of the solid-liquid-vapor (or gas) system whose dissipative minimization constrains the temporal evolution of the phase field. It was shown that the intermolecular force in LBM could be derived from the modified Lennard-Jones potential with hard-core repulsion. The phase interface is represented over several elements, in which the density changes gradually. The profile of the interface is regularized by thermodynamic equilibrium of the free energy, which eliminates the need for artificial numerical dissipation. The wall free energy can take a polynomial form as it describes an attraction of the liquid by the solid and a certain reduction of liquid/liquid attractive interactions near the surface. This partial wetting boundary condition is naturally imposed in the framework of the Galerkin Finite Element method, even in the presence of irregularly patterned surfaces. For these reasons, FE-LBM has certain advantages over sharp interface methods based on Volume-of-Fluid (VOF) or Front Tracking methods; computations are much easier for 3-D flows in which topological change of the interfaces is complicated. FE-LBM is especially useful when phase change is under consideration, since the speed of displacement of the interface must be explicitly computed in sharp interface methods. In addition, FE-LBM is appropriate for some problems that are currently challenging for sharp interface methods such as wetting/dewetting and coalescence of bubbles and droplets.

We have developed a new LB formulation for iso-thermal two-phase flows that is based on a novel “*velocity*” formulation rather than popular and more natural “*momentum*” formulation. Although the velocity based formulation offers significantly better stability (stable up to $Re \sim O(10^4)$ without any special treatment) and thinner liquid-gas interfacial thickness (~ 2 or 2.5 grid spacing), it also presents a problem related to recovering fully consistent Navier-Stokes equations in the thin but finite interfacial region. Major effort has been put into this issue over the past several months and a correction was introduced to the new version of FE-LBM code. We are now validating this version for various two-phase flows involving drops and bubbles with contact line dynamics. A journal paper on the algorithm is in preparation. For high-Reynolds number flow, the Vreman LES model is adopted and has been tested for liquid separation.

A new version of the FELBM code in which the LES-type subgrid turbulence model of Vreman has been implemented was tested for a rotating concentric cylinder case. Parallel scaling of the code was also tested up to 1024 processors with the resulting scaling efficiency (relative to 64 processors) shown in Table 1. Full simulations for the two test

Table 1. Parallel efficiency of FE-LBM solver

# Procs	elements/proc (tot = 2.46M)	Efficiency, % (relative to N = 64)
64	38400	100.0%
128	19200	93.0%
256	9600	92.6%
512	4800	87.0%
1024	2400	58.8%

conditions were performed using 512 processors on the Fission cluster at INL. An all hexahedral mesh consisting of $36 \times 400 \times 360$ elements was used for the test.

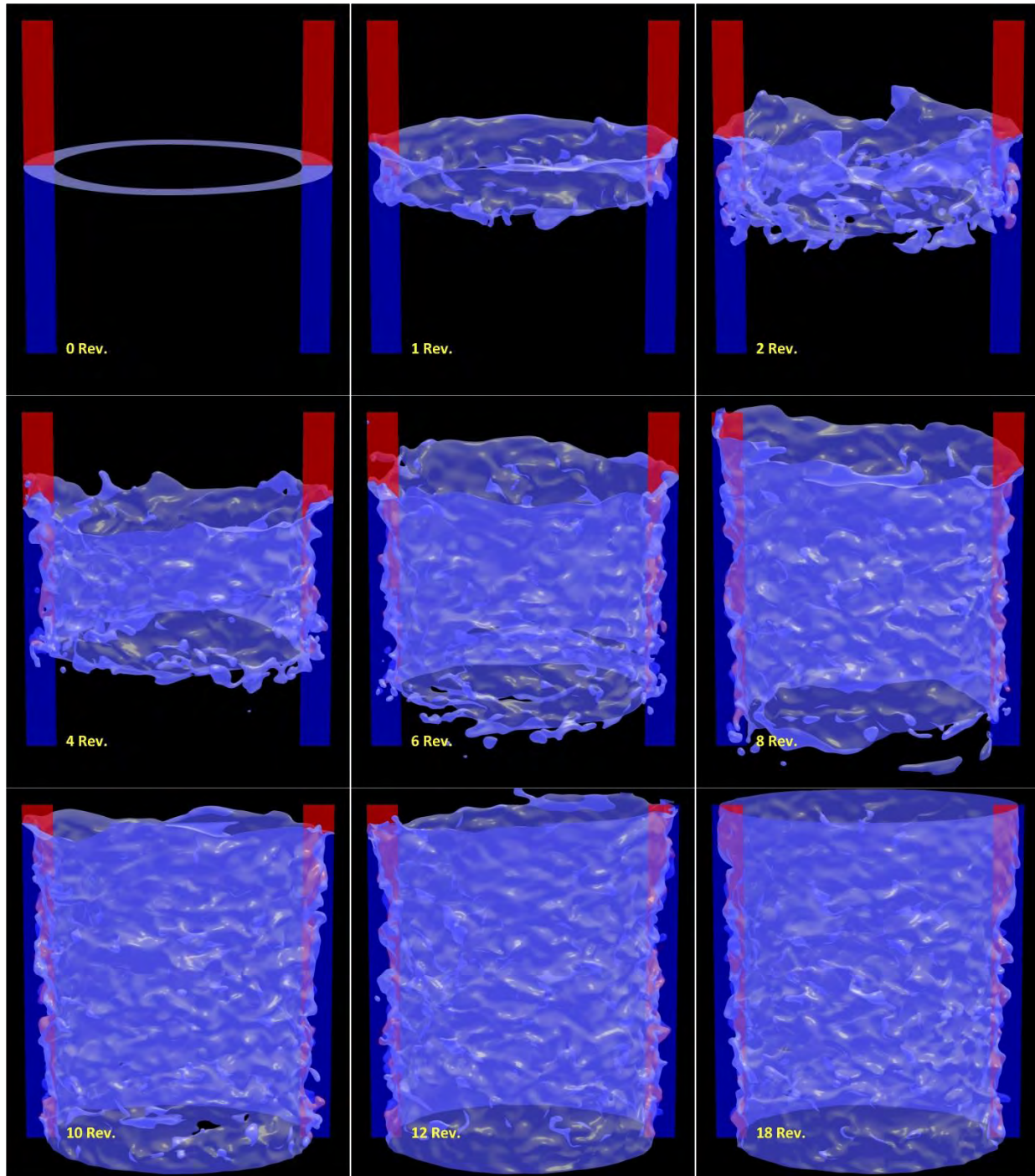


Figure 1: Sequence of free surface evolution inside a concentric cylinder, in which the inner cylinder rotates while the outer cylinder is stationary. Gravity acts in the vertical direction. Blue phase is water and red phase is air. Flow parameters are $Re = 40,000$ ($\sim 2,000$ rpm), $We = 3,250$, and $Fr = 25.5$. Vreman's LES model is incorporated.

Figure 1 shows the sequence of turbulent free surface profiles of the Taylor-Couette flow between a rotating inner cylinder and a stationary outer cylinder at $Re = 40,000$ (equivalent to 2,000 rpm). The Weber number is $We = 3,250$, and the Froude number is $Fr = 25.5$. The simulation begins with zero initial velocity and as the inner cylinder rotates the free surface becomes irregular and pushed away from the inner cylinder due to the centrifugal acceleration. At around 10 revolutions, the interface reaches quasi-steady state. Vreman's eddy viscosity model was employed. It was found that the LES subgrid turbulence model was successful at further stabilizing the solution even at this high Reynolds number, which is well beyond where this solver has been functional in the past. In the figure, significant chaotic vortexing with some predicted entrained air bubbles was found. This result is generally consistent with expectation and future efforts will seek to define the geometry and dimensionless flow variables such that a direct comparison can be made with other dimensional simulations using traditional CFD tools such as OpenFOAM. To get deeper insight into the coalescence of bubbles or drops, we investigated a partial drop coalescence process. When a drop settles gently in an immiscible ambient fluid onto a flat interface between these two fluids, it rests on the interface for an extended time and then coalesces with the homophase beneath the interface. Under certain conditions, the merging between the drop and the lower bulk is not completed at once but goes through many cycles of partial coalescence, each leaving a smaller daughter drop on the interface, which is generally attributed to capillary pinch-off. Scaling relationships have been developed for the size ratio and the coalescence time in terms of the Bond number (Bo) and Ohnesorge number (Oh). Numerical simulations based on a phase-field method carried out using the Adaptive Mesh Refinement technique for nearly equal density and viscosity fluids for the range of Ohnesorge number larger than 0.01. Here we carried out a partial drop coalescence simulation of liquid and air, whose Ohnesorge number is 0.0005 on fixed non-uniform mesh using the new FE-LBM approach. The results are shown in Fig. 2, which predicts partial drop coalescence.

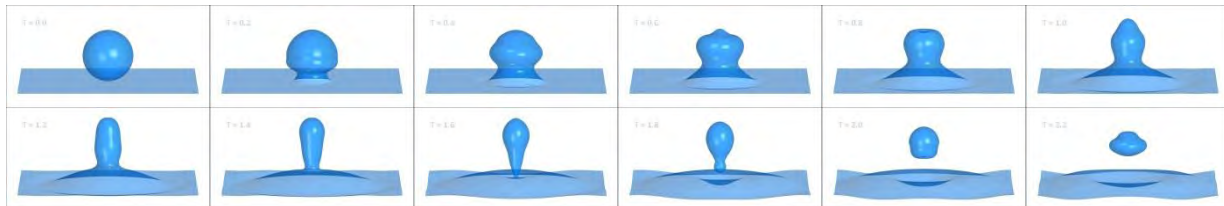


Figure 2: Sequence of a water drop coalescence. $Oh = 0.0005$, $Bo = 0.03$. Time is non-dimensionalized to inertial time scale.

2. Isothermal Single Bubble Rising at High Reynolds Numbers

Two phase gas-liquid flows are encountered in large variety of practical situations, such as petroleum industry for the simultaneous transportation of the oil and natural gas, bubble columns and cooling systems in nuclear power plants. The above mentioned applications required an intensive knowledge of bubble dynamics at moderate to high Reynolds number (Re). Although many numerical simulations have been applied to study the dynamics of single bubble rising. The majority of the numerical investigations of rising bubbles aim at model validation, for this reason in most cases the results are restricted to bubbles rising in a straight path at low to moderate Re . To our knowledge, few numerical examination of unsteady bubble motion have been performed. Although experiments provide considerable insight into the mechanism governing the unsteady motion of the bubble there are distinct discrepancies between available experimental results which can be attributed to a contamination of the liquids. In numerical simulations such effects can be avoided. In addition the high spatial and temporal resolution of the data obtained in simulations allows for a detailed investigation of the unsteady wakes and shape changes in rising bubbles. In this work a detailed study of the path oscillations, shape oscillations, and the unsteady wake dynamics of high Re bubbles is conducted to provide a comprehensive understanding of the bubble dynamics at high Re .

Finite element lattice Boltzmann equation (FE-LBE) method is used to study the dynamics of two dimensional and three dimensional bubbles rising at high Reynolds number ranging from $O(10^2)$ to $O(10^4)$ for a wide range of Archimedes number. The FE-LBE method was proposed by Lee and Lin, in which the LBE is regarded as a special space-time discretization of the discrete Boltzmann equation in the characteristic direction. The streaming step is equivalent to solving a pure linear advection equation for the particle distribution function, thus it can be solved by any higher-order accurate schemes on an unstructured mesh. Decoupling the collision step from the streaming step offers numerical stability at high Reynolds numbers.

The Bond number Bo , Archimedes number Ar , and the Reynolds number Re are the characteristic parameters for this problem. They are defined by

$$Bo = \frac{g\Delta\rho d^2}{\sigma}, \quad Ar = \frac{\sqrt{gd}d}{\nu}, \quad Re = \frac{\rho_l U_t d}{\eta_l}$$

respectively. Here g denotes the gravitational acceleration, $\Delta\rho = \rho_l - \rho_g$ is the density difference between the gas and liquid phases, σ is the surface tension, d is the bubble diameter, η_l is the liquid viscosity, V_t is the bubble terminal velocity.

Results of two dimensional bubbles rising at high Re are presented below. Simulations were performed in a two dimensional computational domain of the size $16d \times 16d$ and resolution 800×800 . Periodic boundary condition is imposed in the vertical direction. The Bubble shape, path and its rise Reynolds number show a good agreement with available experimental and numerical studies.

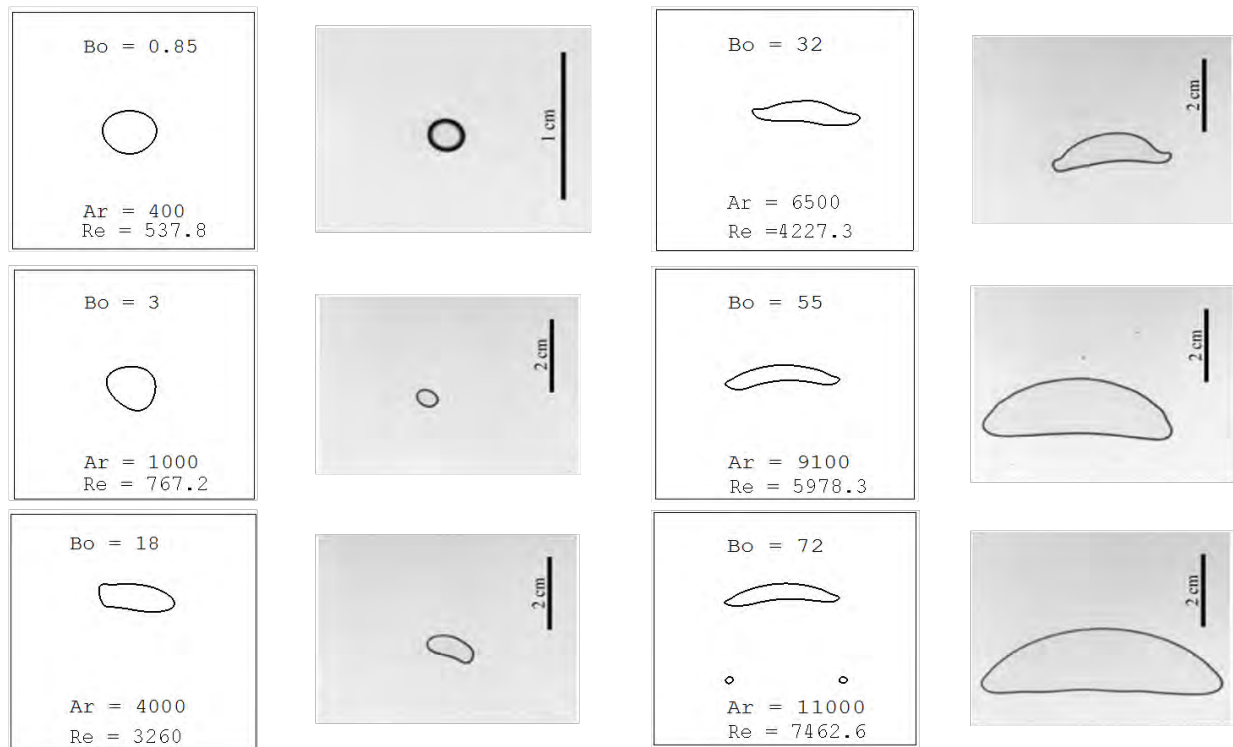


Figure 3: Evolution of the mean shape and Re with Ar and Bo

The left columns in Fig. 3 show the numerical results and the right columns present the experimental results by Roig et al.

3. Development of Novel “Conservative” *Derivative-Free* LBM with Adaptive Mesh Refinement

Continuing our previous efforts in developing an adaptive mesh refinement technique (AMR) for fluid dynamic simulations we present a lattice Boltzmann method (LBM) for immiscible two-phase flows on nonuniform grids. The proposed AMR-LBM is equipped with a multi-relaxation-time (MRT) collision operator to allow attaining high Reynolds numbers. On the other hand, a mass-conserving interface tracking equation is proposed to track the interface between different phases. Various benchmark studies are carried out to validate the model in terms of accuracy and stability.

Conservative phase-field equation

To track the interface between different fluids the following lattice Boltzmann equation

$$\frac{Dh_\alpha}{Dt} = -\frac{h_\alpha - h_\alpha^{eq}}{\lambda_h}$$

is solved in two steps:

Collision:

$$\tilde{h}_\alpha = h_\alpha - \frac{h_\alpha - h_\alpha^{eq}}{\tau_h + 0.5}$$

Advection:

$$\frac{\partial \tilde{h}_\alpha}{\partial t} + \mathbf{e}_\alpha \cdot \nabla \tilde{h}_\alpha = 0$$

where $\tau_h = \lambda_h/dt$ is the dimensionless relaxation time and the equilibrium distribution function is given by

$$h_\alpha^{eq} = \phi \Gamma_\alpha + B w_\alpha (\mathbf{e}_\alpha \cdot \mathbf{n})$$

where

$$\Gamma_\alpha = w_\alpha \left[1 + \frac{\mathbf{e}_\alpha \cdot \mathbf{u}}{c_s^2} + \frac{(\mathbf{e}_\alpha \cdot \mathbf{u})^2}{2c_s^4} - \frac{u^2}{2c_s^2} \right]$$

$$B = \frac{M}{c_s^2} \left(\frac{1 - 4\phi^2}{W} \right)$$

in which ϕ is the phase field, t stands for time, c_s is the lattice speed of sound, w_α is the weight coefficient set, \mathbf{e}_α is the microscopic velocity set, \mathbf{u} is the macroscopic velocity vector, W is the interface thickness, \mathbf{n} is the vector normal to the interface, and the mobility is related to the relaxation time by

$$M = (\tau_h - 0.5)c_s^2 \delta t$$

The above formulations recover the following conservative phase-field equation

$$\frac{\partial \phi}{\partial t} + \nabla \cdot (\phi \mathbf{u}) = \nabla \cdot \left[M \left(\nabla \phi - \frac{(1 - 4\phi^2)}{W} \mathbf{n} \right) \right]$$

The density is linearly interpolated from the computed phase field by

$$\phi = \sum_{\alpha} h_{\alpha}^{eq}$$

$$\rho = \rho_l + (\phi - \phi_{min})(\rho_h - \rho_l)$$

where ρ_l and ρ_h are densities of light and heavy fluids, respectively, and ϕ_{min} is the minimum value of the phase-field variable.

Pressure evolution equation for hydrodynamics

The Lax-Wendroff-based finite-difference LBM (FDLBM) is used to solve the momentum equation. The collision of the pressure evolution equation read as

$$\tilde{g}_{\alpha} = \bar{g}_{\alpha} - \mathbf{M}^{-1} \hat{\mathbf{S}} \mathbf{M} (\bar{g}_{\alpha} - \bar{g}_{\alpha}^{eq}) + \delta t (\mathbf{e}_{\alpha} - \mathbf{u}) \cdot [(\Gamma_{\alpha} - w_{\alpha})(\rho_h - \rho_l) c_s^2 \nabla^M \phi + \Gamma_{\alpha} (\mu \nabla^M \phi + \mathbf{F}_b)]$$

where \mathbf{F}_b is the body force, μ is the chemical potential, and the modified equilibrium distribution function is

$$\bar{g}_{\alpha}^{eq} = g_{\alpha}^{eq} - \frac{\delta t}{2} (\mathbf{e}_{\alpha} - \mathbf{u}) \cdot [(\Gamma_{\alpha} - w_{\alpha})(\rho_h - \rho_l) c_s^2 \nabla^C \phi + \Gamma_{\alpha} (\mu \nabla^C \phi + \mathbf{F}_b)]$$

in which

$$g_{\alpha}^{eq} = \rho c_s^2 (\Gamma_{\alpha} - w_{\alpha}) + p w_{\alpha}$$

After collision, the advection step is carried out using the following Lax-Wendroff scheme

$$\bar{g}_{\alpha}(\mathbf{x}, t + \delta t) = \tilde{g}_{\alpha}(\mathbf{x}, t) - \sigma [\tilde{g}_{\alpha}(\mathbf{x}, t) - \tilde{g}_{\alpha}(\mathbf{x} - \Delta \mathbf{x}_{\alpha}, t)]$$

$$- \frac{1}{2} \sigma (1 - \sigma) [\tilde{g}_{\alpha}(\mathbf{x} + \Delta \mathbf{x}_{\alpha}, t) - 2\tilde{g}_{\alpha}(\mathbf{x}, t) - \tilde{g}_{\alpha}(\mathbf{x} - \Delta \mathbf{x}_{\alpha}, t)]$$

where $\sigma = \frac{e_{\alpha} \delta t}{\Delta x_{\alpha}}$ is the CFL number and Δx_{α} is the grid spacing in the direction of \mathbf{e}_{α} . The macroscopic properties are calculated by

$$\mathbf{u} = \frac{1}{\rho c_s^2} \left(\sum_{\alpha} \bar{g}_{\alpha} \mathbf{e}_{\alpha} + \frac{\delta t}{2} \mu \nabla^C \phi \right)$$

$$p = \sum_{\alpha} \bar{g}_{\alpha} + \frac{\delta t}{2} (\rho_h - \rho_l) c_s^2 \mathbf{u} \cdot \nabla^C \phi$$

Numerical results

1. Rising bubble under buoyancy force

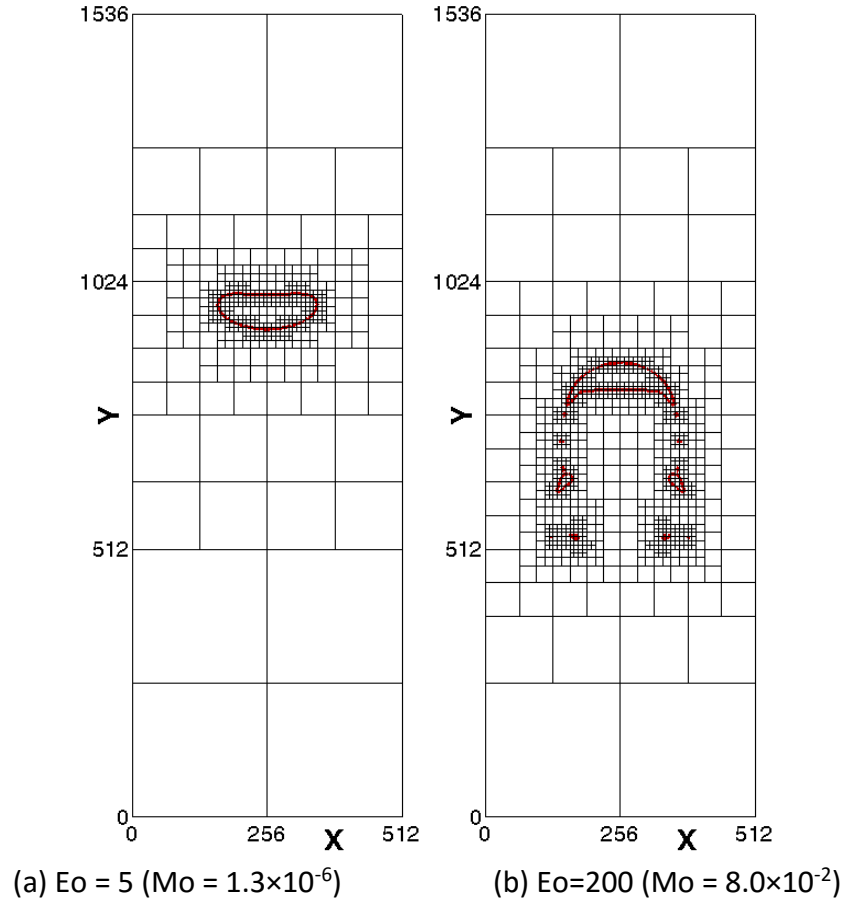


Figure 4: AMR-LBM simulations of rising bubble under buoyancy force.

Here, we consider the motion of a bubble in a rectangular channel. Initially, a circular bubble with diameter $D = L_0/5$ is placed at $(L_0/2, L_0/2)$ in a rectangular domain of length L_0 and height $3L_0$. The link bounce-back boundary condition is applied at the bottom and top, and the lateral boundaries are periodic. The density and viscosity ratios are fixed at $\rho_h/\rho_l = 1000$ and $\mu_h/\mu_l = 100$, respectively, and the results are presented in terms of Eötvös and Morton numbers. As it can be seen in Fig. 4, at low Eötvös numbers the bubble is less deformed while increasing the Eötvös number causes the bubble to deform more and eventually, at a large enough Eötvös number, the skirt breakup is observed. In all the simulations the interface is very well resolved using the structured AMR blocks.

2. Falling droplet under buoyancy force

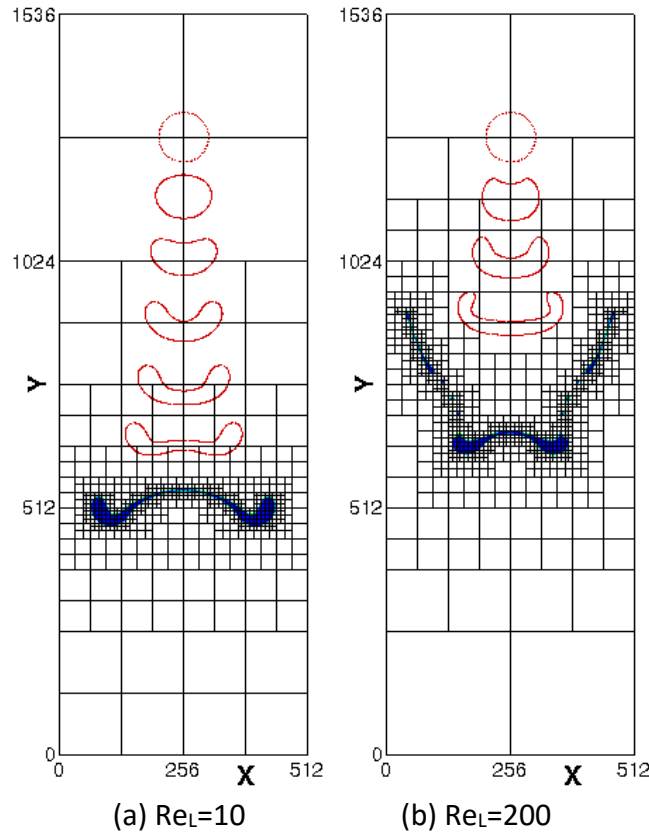


Figure 5: Onset of the bag breakup and multimode breakup of a droplet falling due to gravitational force.

Now we place a liquid droplet with diameter $D = L_0/5$ at $(L_0/2, 3L_0/2)$ and track its evolution as it falls due to the gravitational effects. The computational domain and the boundary conditions are the same as in the rising bubble simulations. Two sets of simulations are conducted at a moderate density ratio $\rho_h/\rho_l = 10$ with $Eo=100$ and $Re_G=20$. In the first case $Re_L=10$ and the evolution of the drop as it falls due to the body force is depicted in Fig. 2(a). The formation of a bag-shaped droplet can be seen and the drop undergoes a bag-breakup mechanism. The results for the second case with $Re_L=200$ are shown in Fig. 5(b). It is observed that the drop is undergoing a multimode breakup mechanism. The multimode breakup is a combination of the bag breakup and shear breakup modes and occurs when the droplet viscosity is low enough and the drop-based Reynolds number is within a certain range, which is the case in Fig. 5(b). A closer snapshot of the bag breakup and multimode breakup mechanisms is shown in Fig. 6. As it can be observed, the AMR results are quite successful at capturing small satellite droplets without a major difficulty.

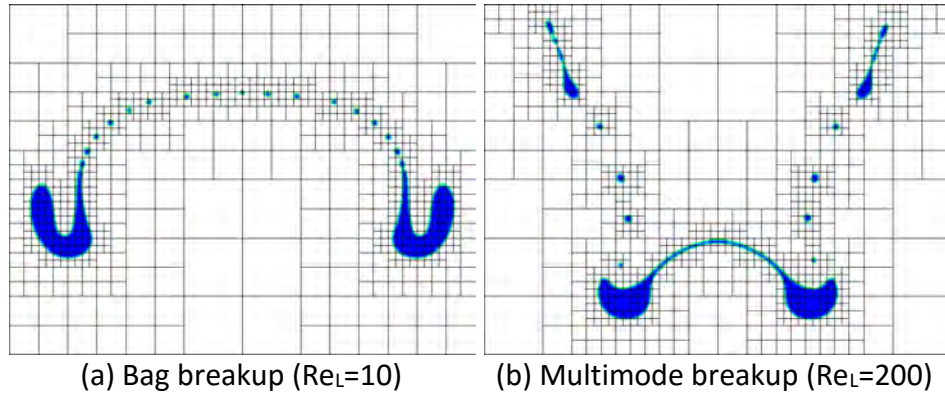
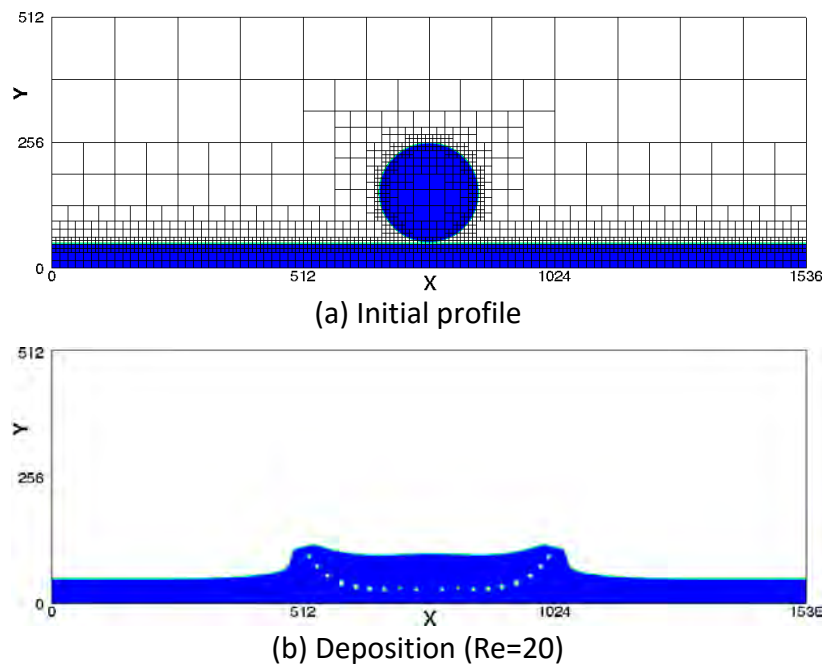


Figure 6: Different breakup mechanisms of a falling droplet.

3. Droplet splashing on a wet surface

Drop impact on a wet surface poses interesting dynamics and its simulation is very challenging because in addition to large density and viscosity difference across the interface of the two fluids there is a singularity at the impact point. Here we choose this problem to show the versatility of our proposed AMR-LBM model in tackling this phenomenon.

We conduct the simulations for two sets of parameters at low and moderate Reynolds numbers corresponding to the deposition and splashing mechanisms, respectively. The density ratio and Weber number are fixed at 1000 and 8000, respectively. In the first case $Re=20$ ($\mu_h/\mu_l=1000$) while in the second case $Re=100$ ($\mu_h/\mu_l=200$). The deposition and splashing states shown in Fig.7 are in good agreement with previous studies.



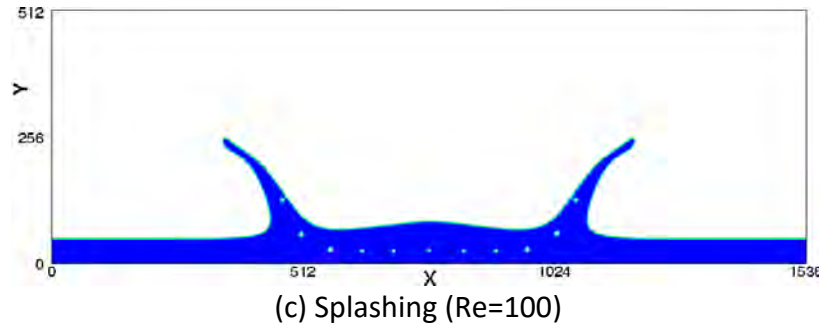
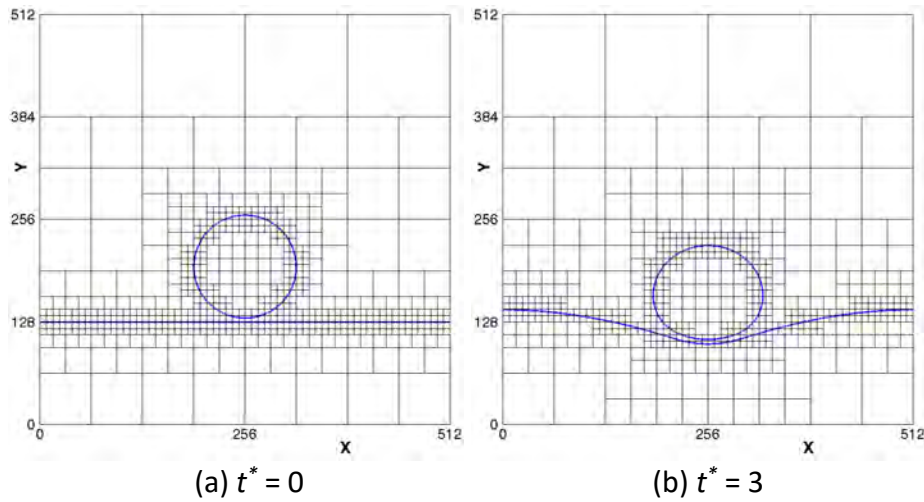
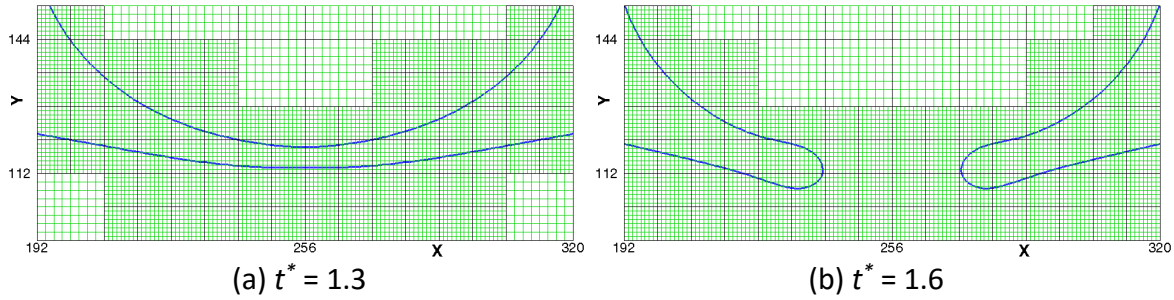


Figure 7: Drop splashing on a wet surface.

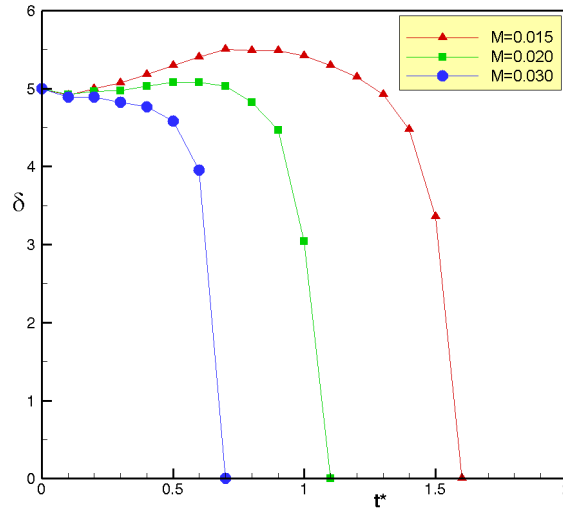
4. Droplet coalescence onto a fluid interface

Figure 8: Droplet under gravity sitting on top of a flat interface ($M=0.010$).

A droplet placed in the vicinity of a flat interface can exhibit different behaviors depending on the overriding factors characterized by gravitational forces, viscous stress, and capillary pressure. In addition to density and viscosity contrasts, the important dimensionless groups are the Bond number and the Ohnesorge number. Here, we consider the effects of mobility and interfacial thickness on the quality of droplet coalescence onto the flat interface. We choose the parameters such that $\rho_h/\rho_l=1.2$, $\mu_h/\mu_l=1$, $Bo=0.8$, and $Oh=0.08$. Initially, a droplet with radius $R=L_0/8$ is placed at $(L_0/2, H+R+\delta)$ inside a computational domain of size $L_0 \times L_0$, where $H=L_0/4$ is the height of the fluid bath beneath the droplet and $\delta=5$ is the gap between the droplet interface and the fluid bath. The boundary conditions are link bounce-back at the bottom and top of the domain and periodic in the x-direction. Fig. 8 shows the evolution of the drop with $W=3$ and $M=0.01$. We chose a relatively low value for the mobility to capture the moment that the droplet sits steady on top of the deformed interface. A close up of the displacement between the droplet and the deformed interface can be seen in Fig.9 for $W=3$ and $M=0.015$.

Figure 9: Droplet coalescence onto a flat interface ($M=0.015$).

The effect of the mobility on the instant of coalescence between the droplet and interface is shown in Fig.10. As expected, the droplet merges onto the fluid bath earlier at higher mobility values. In our simulations we found that increasing the interface thickness also expedites the coalescence.

Figure 10: Droplet coalescence onto a flat interface ($M=0.015$).

5. Kelvin-Helmholtz instability

In our recent study, we examined the Kelvin-Helmholtz instability (KHI) of a stratified shear layer for both single-phase and multiphase flows on a uniform mesh. We also examined the single-phase KHI on nonuniform grids using AMR-LBM and obtained reasonably accurate results. In this section, we consider the KHI of a two-phase shear-layer flow for both density-matched binary fluids and two immiscible fluids with a density contrast using the proposed AMR-MRT-LBM. The results can be presented in terms of four dimensionless groups: density ratio, Weber number, and two Reynolds numbers based on the properties of the light and heavy fluids. Initially, a uniformly concentrated vorticity distribution in the form of the Dirac delta function is imposed to the entire fluid.

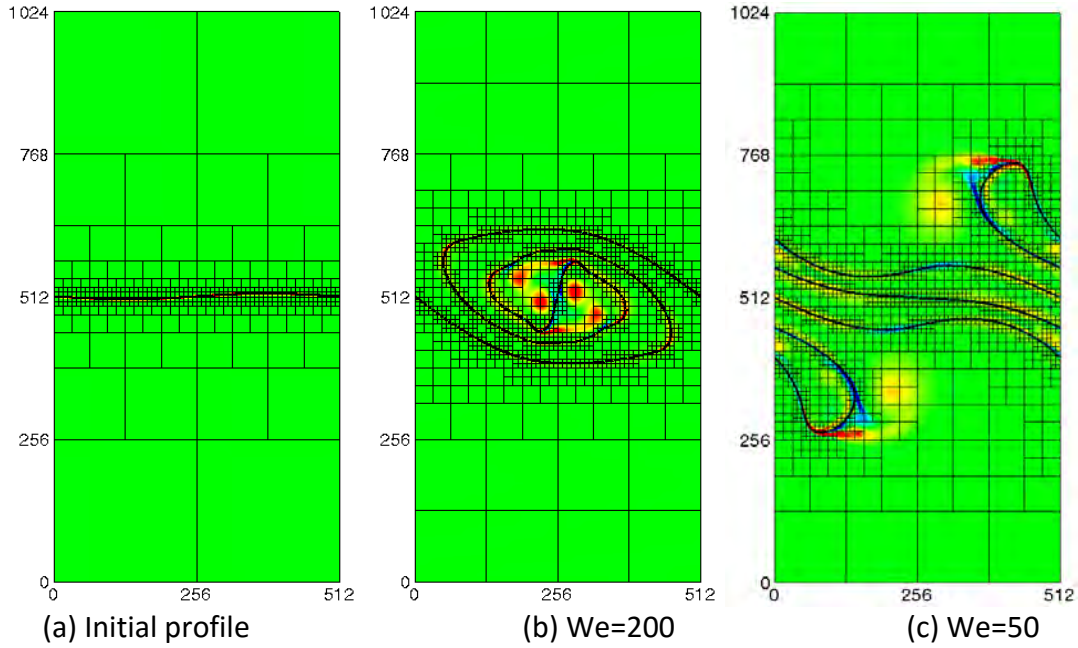
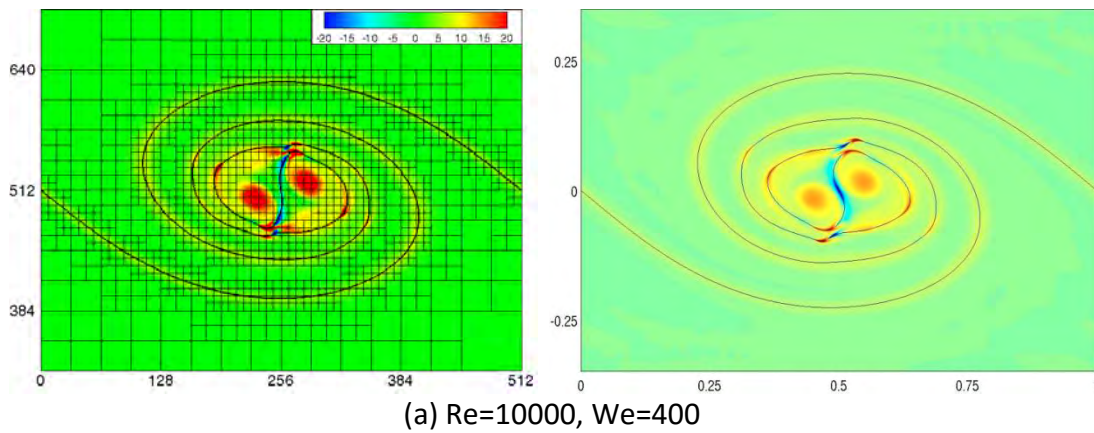


Figure 11: Kelvin-Helmholtz instability of two immiscible fluids at $Re_l = Re_h = 20000$.

First, we consider density-matched immiscible fluids at high Reynolds numbers $Re_l = Re_h = 20000$. The initial configuration of the AMR blocks together with the interface location and vorticity contours for two different Weber numbers are shown in Fig. 11. As it can be seen in Fig. 11(b), a symmetric interface roll-up is observed for $We=200$ while at a lower Weber number in Fig. 11(c) fingers of interpenetrating fluids is created, which is in line with the previous observations.



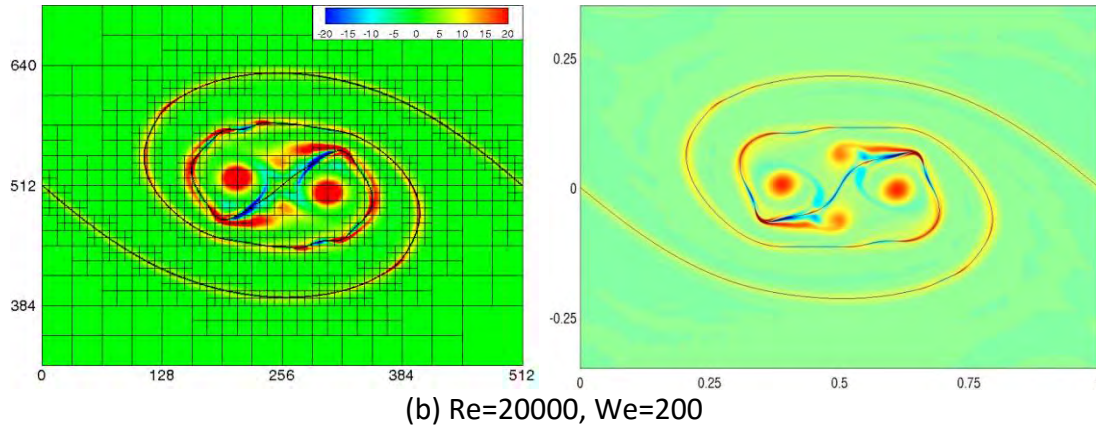


Figure12: Kelvin-Helmholtz instability of two immiscible fluids. Left: AMR-LBM; Right: benchmark [6].

We also considered the effect of density ratio on the interface roll-up pattern. We examined three different density ratios at $Re_l=Re_h=10,000$ and the results are shown in Fig. 12. As can be seen, increasing the density ratio at a constant Reynolds number results in a chaotic interface evolution and turbulence in the flow field. This is due to the fact that at larger density ratios the inertial force of the heavy fluid dominates the viscous forces causing a highly deformed interface and eventually catastrophic breakup of the interface. Also, it is noticed that flow field is no longer symmetric for the fluids with different densities.

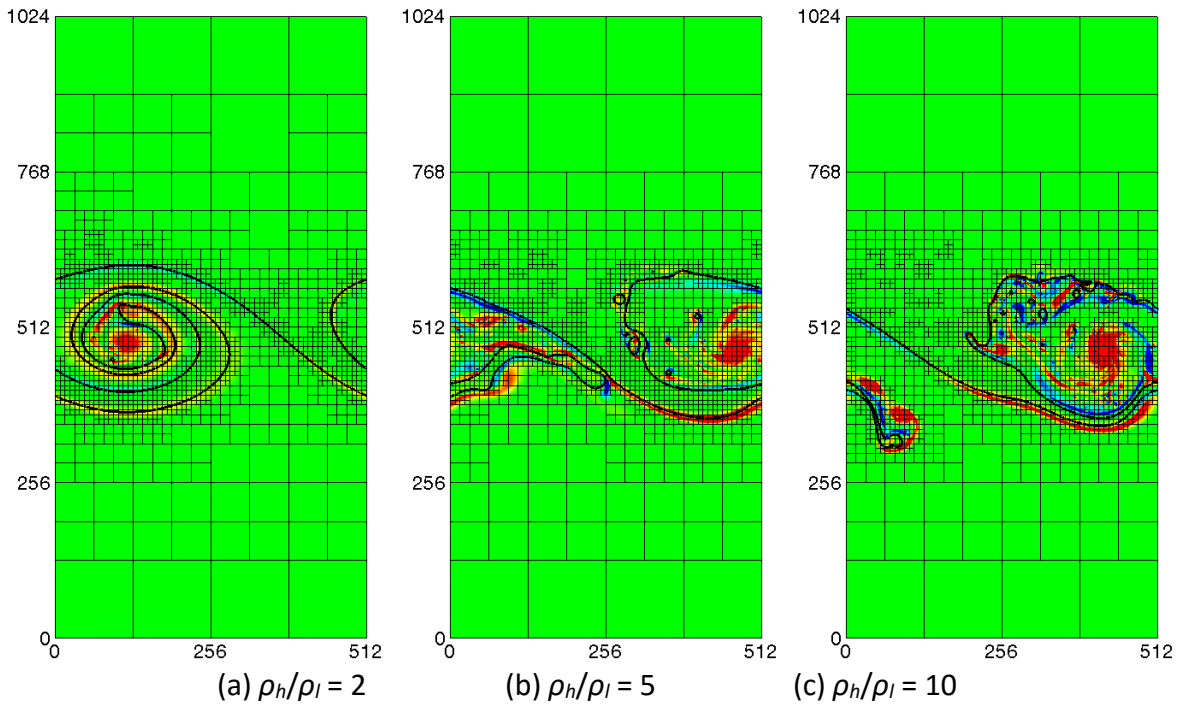


Figure 13. Vorticity (flooded contour) and interface location (black line) of a two-phase shear flow.

4. Thermal Two-phase Lattice Boltzmann Model

The multiphase Lattice Boltzmann equation method introduced by the PIs is modified to include boiling phenomena. The boiling effect is considered by including non-zero divergence of velocity in the pressure evolution equation. Compared with the existing thermal LBM models, our thermal LBM is stable at lower temperature and pressure (i.e., larger saturation density ratio), and free of tunable parameters.

Problem Description: Nucleate Boiling

In this section the two-dimensional nucleate boiling phenomena is simulated using the proposed multiphase LBE method. The computational setup is shown in Fig. 14. Initially, a vapor bubble is sitting at the center of bottom hot wall with initial equilibrium contact angle ($\theta = 53^\circ$). The color contours shows the density distribution. The bottom boundary is wall, the top boundary is open to let the liquid exists freely due to the volume expansion, and the left and right boundaries are periodic in horizontal direction. Depending on the computational setup, the left and right boundaries can be considered either symmetric or periodic. This problem is different from the film boiling case since both the liquid and vapor phase touches the bottom wall initially and during the simulation time. The gravity ($g=9.81 \text{ m/s}$) is also acting in the vertical direction.

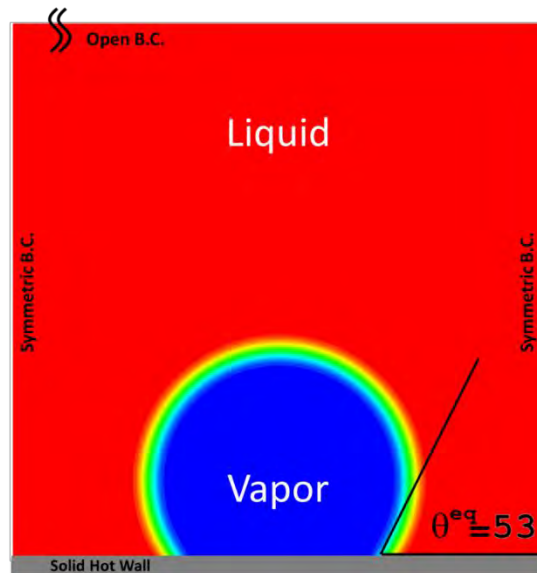


Figure 14: Schematic of the two-dimensional nucleate boiling problem.

This problem is very close to real boiling. The bottom wall is kept at temperature higher than the liquid saturation temperature ($T_w = T_{sat} + \Delta T$). The excess temperature considered is $\Delta T = 5$. Once the liquid-vapor interface feels the superheat, the phase change occurs and vapor volume increases. Since the bulk fluids are considered incompressible, the liquid exists from the top boundary with no friction. As the vapor bubble grows in size, the liquid move downward from the sides due to the buoyancy force. At some point the vapor bubble detaches from the solid wall

and rises vertically. Very close to the solid wall, the heat transfer mechanism is dominated by conduction heat transfer and in the bulk the dominated mechanics is the convection heat transfer. The vapor bubble growth and departure continues and the important parameters are the bubble departure frequency and size.

For the initial vapor bubble density distribution, a profile close to equilibrium based on the initial contact angle is defined. The center of vapor bubble (x_0, y_0) is defined in the Fig. 15.

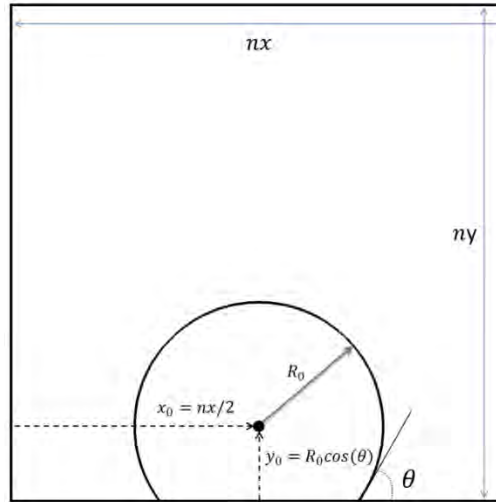


Figure 15: Initial vapor bubble profile.

By defining the initial profile close to equilibrium, the initial deformation toward the equilibrium is minimized and so the stability is increased in case of large density ratios. The liquid and vapor properties are listed in Table 1:

Table 1: Thermophysical properties and non-dimensional parameters in nucleate boiling problem.

Density Ratio	Viscosity Ratio	Eötvös Number	Morton Number	Jakob Number	Peclet Number
ρ_{ratio}	μ_{ratio}	Eu	M	Ja	Pe
40	40	1	7.69E-3	0.071	4.39

The non-dimensional numbers are defined as:

- Eötvös Number, $= \frac{g(\rho_L - \rho_G)l_0^2}{\sigma}$, is the ratio of gravitational to surface tension force.
- Morton Number, $M = \frac{g(\rho_L - \rho_G)\mu_L^4}{\rho_L^2 \sigma^3}$, is a dimensionless number used together with the Eötvös number to characterize the shape of vapor bubble moving in a surrounding liquid.

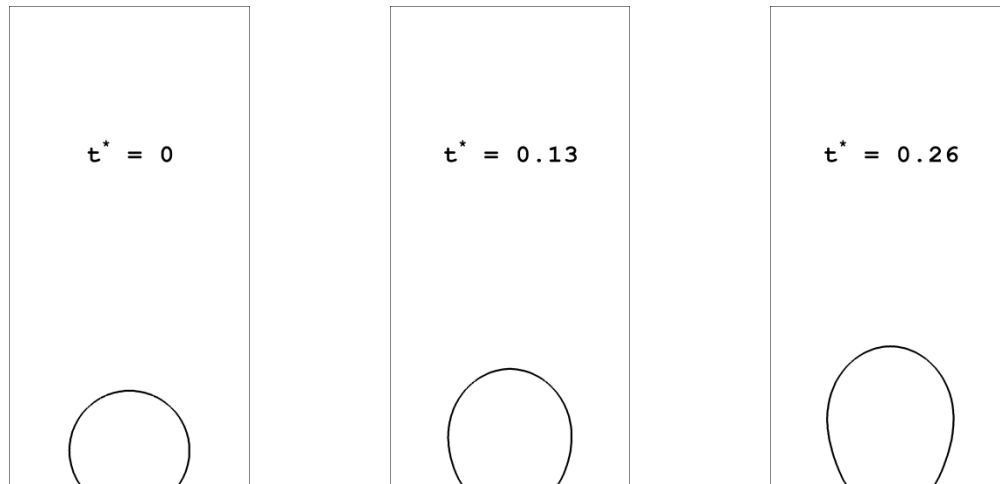
- Jakob Number, $Ja = \frac{c_{pL}(T_w - T_{sat})}{h_{fg}}$, is the ratio of sensible heat to latent heat.
- Peclet Number, $Pe = \frac{\rho_L U_0 l_0 c_{pL}}{k_L}$, is the ratio of convection to conduction heat transfer.

The initial temperature distribution is defined in a way that the vapor bubble is kept at saturation temperature (T_{sat}) and a linear temperature from saturation temperature (T_{sat}) to wall temperature (T_w) is defined between top and bottom boundaries. During the simulation the vapor is kept in saturation temperature by either solving the energy equation in the liquid phase only or considering a very small value for thermal diffusivity of vapor.

Numerical Results

Case 1 – Boiling In Presence of Gravity

In this section a full case of two-dimensional nucleate boiling in presence of gravity is considered in order to test the model capability in to simulate a real boiling case. The time snap shots of density counters at different time steps are shown in Fig. 6. In presence of gravity, there is a delicate balance between the vapor generation at the interface due to phase change and the vapor removal due to buoyancy force. At some point the vapor bubble detaches from the hot wall. The vapor bubble growth behavior on a superheat wall is different from the vapor bubble growth in the superheated liquid since in the former case there is no symmetric condition and temperature uniformity in the surrounding superheated liquid.



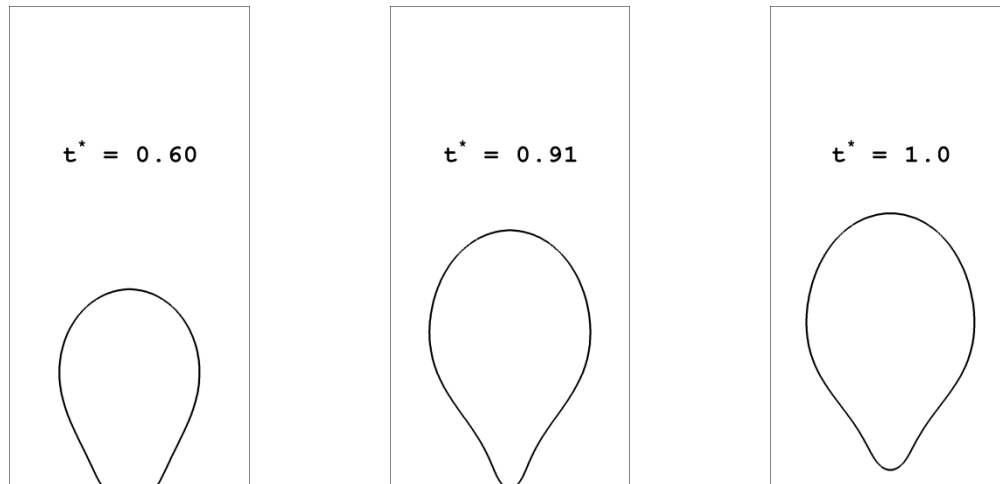


Figure16: Vapor bubble shape at different time steps during nucleate boiling (Case 2).

As can be seen in Fig. 16, at initial times ($t^* = 0.13$), the vapor bubble grows in nearly hemispherical shape. The part of vapor bubble in contact with hot wall is not expanding since the initial profile is very close to equilibrium profile. In the numerical results of Ryu and Ko for the same nucleate boiling problem but slightly different physical and non-dimensional parameters, in the same plot for vapor bubble growth history, the vapor bubble base is expanding because the initial profile is defined by contact angle $\theta = 90^\circ$ instead of $\theta = 53^\circ$ (Fig. 17) and it has a semispherical shape.

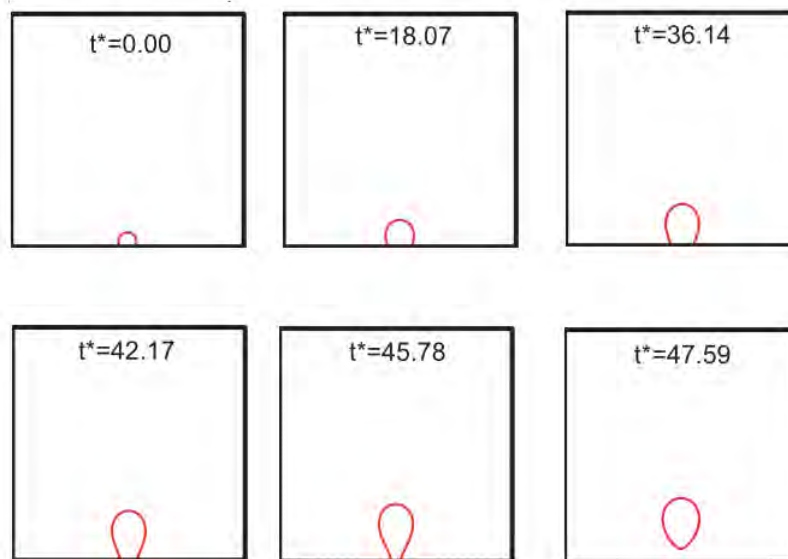


Figure 17: [Ryu and Ko (2012)] Vapor bubble shape at different time steps during nucleate boiling.

The microlayer evaporation is not considered in this study since it can only be resolved using very fine lattice grids. The microlayer is a thin liquid film forms between the vapor bubble contact line

and the hot wall and it is observed in many experimental studies. As the vapor bubble grows in size, the pressure difference inside and outside of it decreases by considering the Laplace law:

$$\Delta p = \frac{\sigma}{R}$$

By further decreasing the pressure difference the vapor bubble tends to get a spherical shape. During the boiling process, the vapor bubble favors attaching to the hot wall because of the contact line. Once the buoyancy force due to gravity overcomes the adhesion force of vapor bubble to the hot wall, the bubble detaches from the wall as shown in the last frame in Fig. 16. The numerical results of Ryu and Ko in (Fig. 17) and the current results (in Fig. 16) show a same trend in terms of vapor bubble growth and detachment from the hot wall. Same trend is also observed in the experimental results of Mukherjee (2004) as shown in Fig. 18.

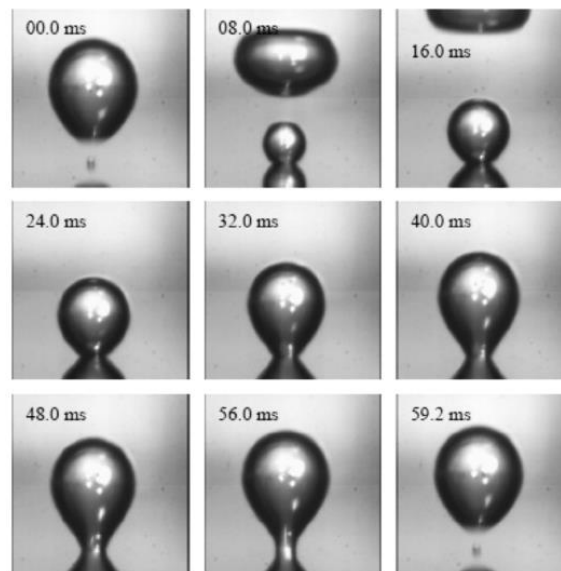


Figure 18: [Mukherjee (2004)] Vapor bubble shape at different time steps during nucleate boiling; experimental study.

The velocity vectors, the vortex ring, and its wakes is shown in Fig. 19 right before the vapor bubble departure from the hot wall. The vortex ring causes the cold liquid on top of the vapor bubble to move downward toward the hot wall. This process is called transient heat conduction which has larger value of heat transfer coefficient compared to natural convection (Carey 1992). This is the reason that nucleate boiling phenomena has larger value of heat transfer coefficient compared to other cooling methods.

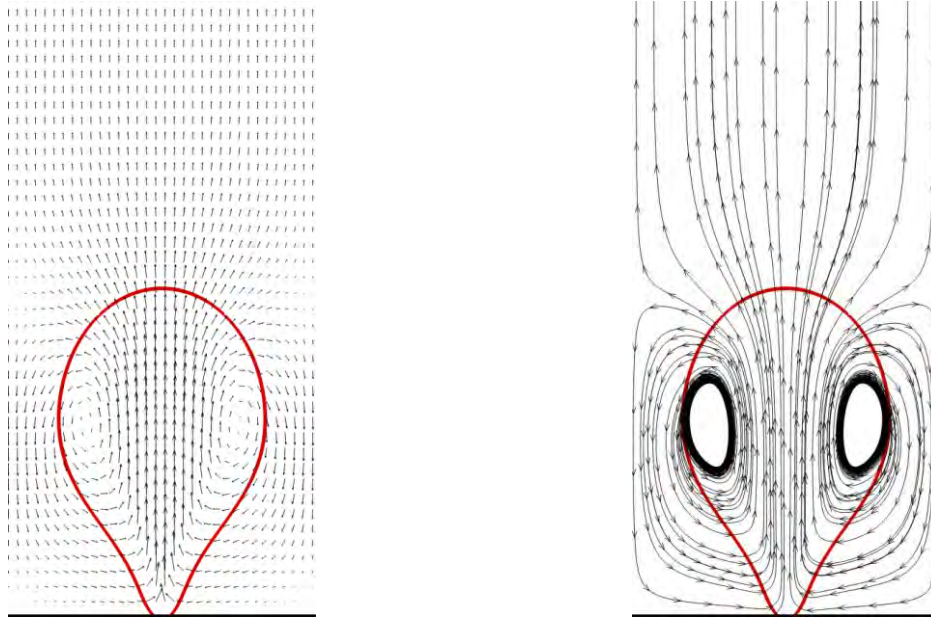
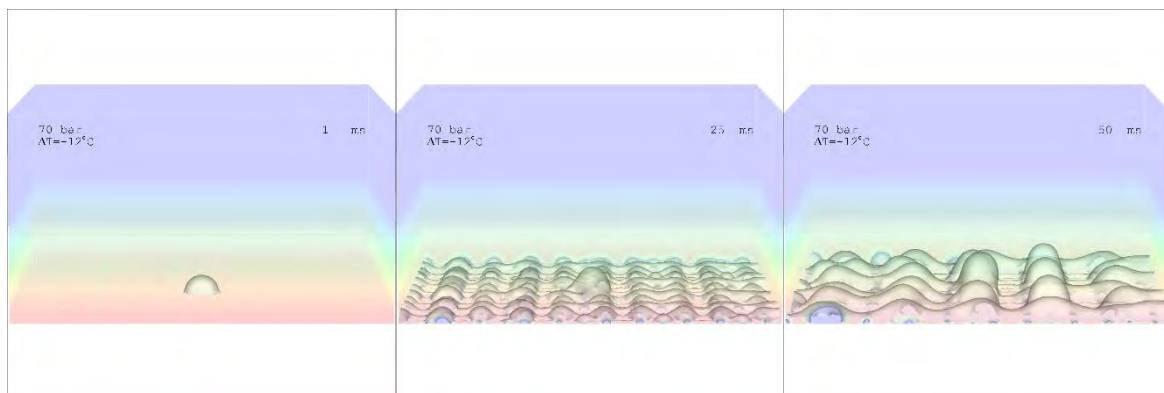


Figure 19: Left: Density contour, velocity vectors, and the vortex ring generated before the vapor bubble departure; Right: Density contours and streamlines ($t^* = 0.91$).

Case 2 – Nucleate Boiling Simulations in PWR condition

The proposed algorithm is tested with the OpenMP parallel code to simulate nucleate boiling on a heated surface with randomly distributed hot spots. These hot spots have stronger affinity to vapor phase so that they are preferred as nucleation sites where bubbles tend to grow. The flow properties such as density/viscosity ratios and surface tension are taken for water and its own vapor at 70 bar. The simulation was performed on 64-core linux cluster.



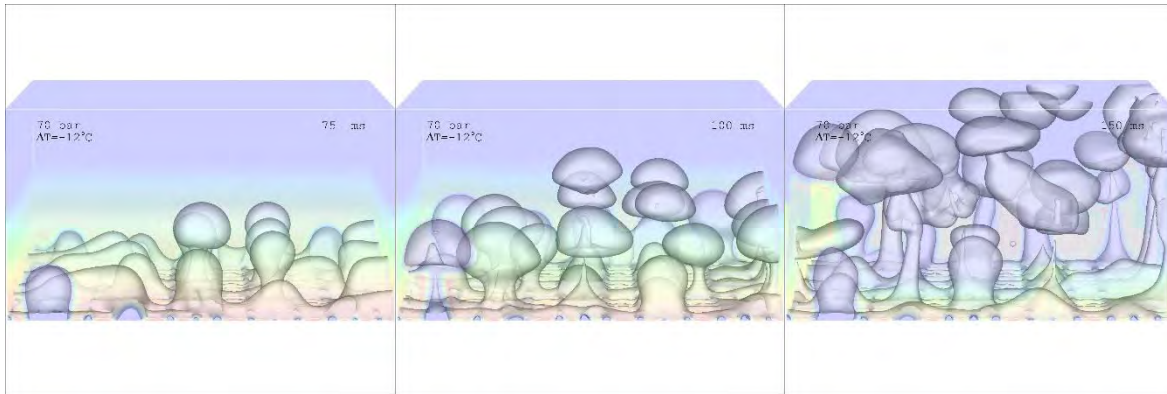


Figure 20: Time evolution of bubble generation and departure from a heated surface with conjugate heat transfer. Initially, the fluid has 12°C subcooling. Color represents the temperature contours.

5. Development of Two-phase NEK-LBM

We describe the latest developments in formulating the NEKLBM solver for conjugate heat transfer and multi-phase flow applications. NEKLBM is a novel CFD solver based on the Spectral-Element Discontinuous Galerkin-Lattice Boltzmann Method (SEDG-LBM) and is able to resolve nearly incompressible single-phase flows using discrete hexahedral elements.

CONJUGATE HEAT TRANSFER

In recent months, we have studied conjugate natural convection in a horizontal annulus. The schematic for problem is given in the following figure:

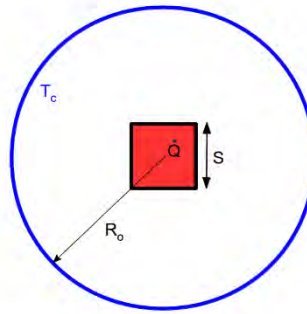


Figure 21: Schematic for the problem

The inner region is a heat generating solid with a square cross-section and side length of S . The outer circular boundary is maintained at a constant temperature T_c , which represents our reference temperature T_o . No-slip boundary conditions are imposed on the inner solid and outer boundaries. Initial conditions reflect a quiescent fluid where the temperature in the entire domain is T_c .

We characterize natural convection flows with two non-dimensional numbers, the Grashof (Gr) and the Prandtl (Pr) numbers. They are defined as follows:

$$Gr = \frac{\beta |g| (\Delta T) L^3}{\nu_f^2} \quad Pr = \frac{\nu_f}{\chi_f} \quad \Delta T = \frac{\dot{Q} R_o^2}{\kappa_f}$$

where the subscript f refers to the fluid properties of viscosity, thermal diffusivity and conductivity. \dot{Q} represents the volumetric heat source arising in the solid.

Numerical Results

The figures below shows the steady-state isotherms and streamlines for $Gr = 10^5$ and 10^6 . The isotherms for $Gr = 10^5$ look nearly concentric about the center of the square, suggesting a conduction dominated effect. In addition, streamlines are symmetric about the vertical axis

revealing a kidney-shaped profile with the center of the streamlines located near the mid-horizontal plane. As the Gr number is increased to 10^6 , the center of the streamlines move upwards and closer to the top of the annulus while symmetry is preserved. Isotherms now exhibit a plume-like structure emanating from the top of the square. Closely packed isotherms near the upper part of the outer cylinder and the lower part of the inner square suggest larger temperature gradients in these areas.

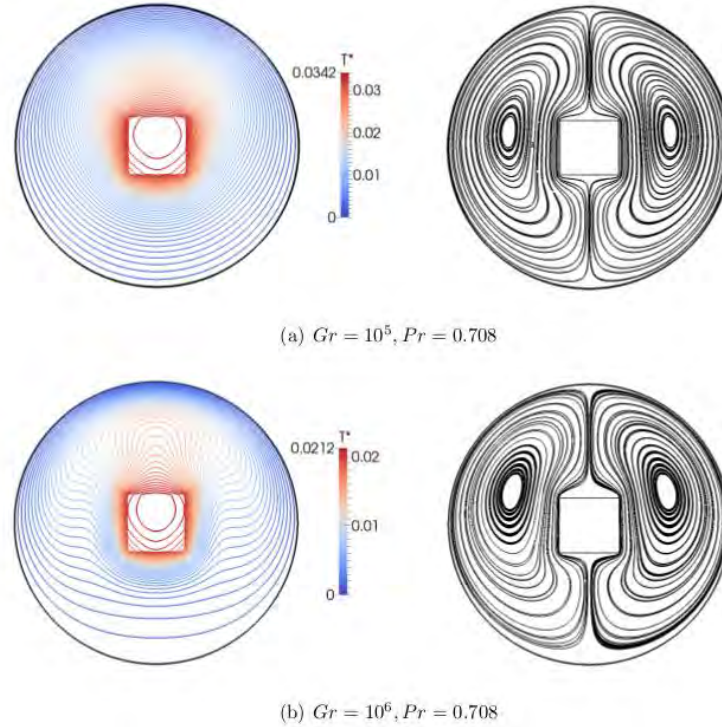


Figure 22: Isotherms and streamlines around a square cylinder

As a means of further investigating the increased temperature gradients, we compute the average Nusselt number of the inner boundary, $Nu_{av,ib}$ and compare results to the work done by Sambamurthy et al. The table below shows Nusselt number calculations for $Gr = 10^5$ and $Gr = 10^6$. As expected, the higher Nusselt number for $Gr = 10^6$ is due to the smaller thermal boundary layer that results from increased convection of flow. The results show the convergence of our scheme as polynomial order is increased from $N = 3$ to $N = 9$. The results agree well with Sambamurthy *et al.* and show reasonable accuracy at low polynomial order ($N = 3$).

Table 2: Convergence of the SE-DG LBM

SEDG-LBM (N)	$Gr = 10^5$	$Gr = 10^6$
3	3.08	4.85
5	3.07	4.95
7	3.07	4.97
9	3.07	4.98
Sambamurthy <i>et al.</i> [27]	≈ 3.00	≈ 5.00

LIQUID-VAPOR TWO-PHASE FLOWS

In this report, we describe the latest developments in formulating the NEKLBM solver for multi-phase flow applications. NEKLBM is a novel CFD solver based on the Spectral-Element Discontinuous Galerkin-Lattice Boltzmann Method (SEDG-LBM) [1] and is able to resolve nearly incompressible single-phase flows using discrete hexahedral elements.

TWO-PHASE FLOWS (Elimination of Parasitic Currents)

We also revisit earlier work on eliminating parasitic currents from multi-phase calculations. The results below are based on a re-scaled version of the intermolecular model proposed by Lee and Fischer [2]. The essential idea is to eliminate terms of order, $O(\mathbf{u}^2)$, or higher from the forcing term. The modified lattice Boltzmann equation becomes:

$$\begin{aligned}\bar{f}_\alpha(\mathbf{x}, t) &= \bar{f}_\alpha(\mathbf{x} - \mathbf{e}_\alpha \delta t, t - \delta t) - \frac{1}{\tau + 1/2} (\bar{f}_\alpha - \bar{f}_\alpha^{eq})|_{(\mathbf{x} - \mathbf{e}_\alpha \delta t, t - \delta t)} \\ &+ \delta t Q_{\alpha, i}|_{(\mathbf{x} - \mathbf{e}_\alpha \delta t, t - \delta t)}.\end{aligned}$$

where

$$Q_{\alpha, i} := [(\mathbf{e}_\alpha \cdot \mathbf{u})\mathbf{e}_\alpha - \mathbf{u}c_s^2] \cdot \nabla \rho \frac{t_\alpha}{c_s^2} - [(\mathbf{e}_\alpha \cdot \mathbf{u})\mathbf{e}_\alpha - \mathbf{u}c_s^2] \cdot \rho \nabla \mu \frac{t_\alpha}{c_s^4}$$

The mass and density are recovered via:

$$\rho = \sum_{\alpha=0}^{N_\alpha} \bar{f}_\alpha \quad \text{and} \quad \rho \mathbf{u} = \sum_{\alpha=0}^{N_\alpha} \mathbf{e}_\alpha \bar{f}_\alpha$$

We show some preliminary results for a static 2D drop (i.e. liquid in vapor). The schematic below shows the geometry for this problem:

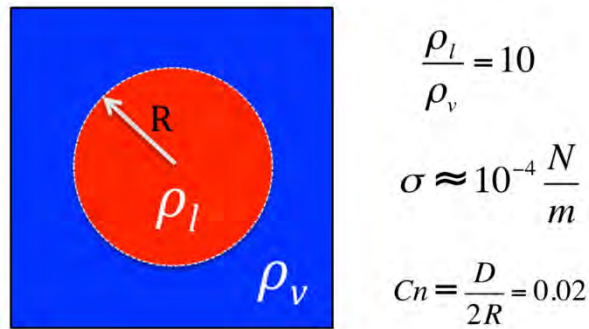


Figure 23: Schematic of the problem

Numerical Results

The density ratio is 10. The interface thickness is $D = 4\Delta x_{\min}$. Where Δx_{\min} is determined based on the spectral element mesh. The following results are based on a uniformly distributed 32×32 element mesh with polynomial order $N = 5$ on the $[-1, 1]^2$ computational domain. Radius of the drop is $R = 0.5$. This gives the following for the surface tension coefficient, $\sigma \approx 10^{-5}$. Cahn number is approx. $Cn = D/(2R) = 0.02$. Fig.24 below shows the steady state parasitic currents for three different schemes. Each scheme solves the streaming step in a different way. The first scheme (described above) is called the modified force in streaming step, or the MFS scheme for abbreviation. The second scheme is a well-known scheme proposed by He, Shan and Doolen, or the HSD scheme. The third scheme is called the force in streaming scheme or the FS scheme for abbreviation. Parasitic currents using the MFS scheme (left image) are practically diminished to machine-precision.

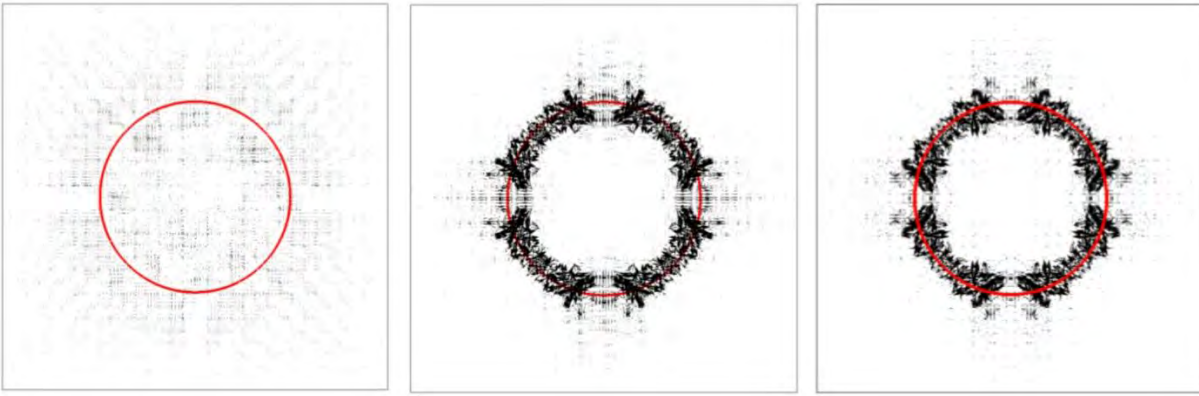


Figure 24: Steady state parasitic currents for 3 different schemes.

We also test the MFS scheme on a non-uniform mesh (see Fig.25 below).

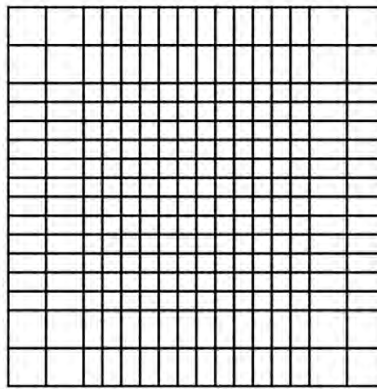


Figure 25: Nonuniform mesh

On this mesh, we employ polynomial order of $N = 7$ for a stationary drop with interface thickness of $D = 0.05$. Fig. 26 below shows the time evolution of the maximum kinetic energy for variable β and for variable relaxation times, τ . The time is non-dimensionalized to the viscous time of the vapor phase. In both cases, the maximum kinetic energy diminishes exponentially to round-off with time.

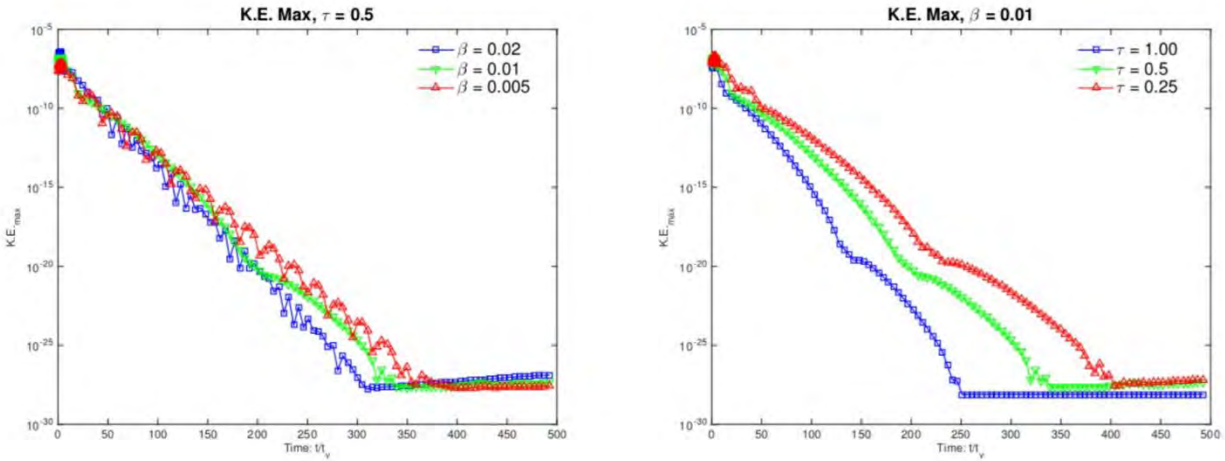


Figure 26: Time evolution of the maximum kinetic energy

We also show convergence of the Young-Laplace pressure law in the figure below:

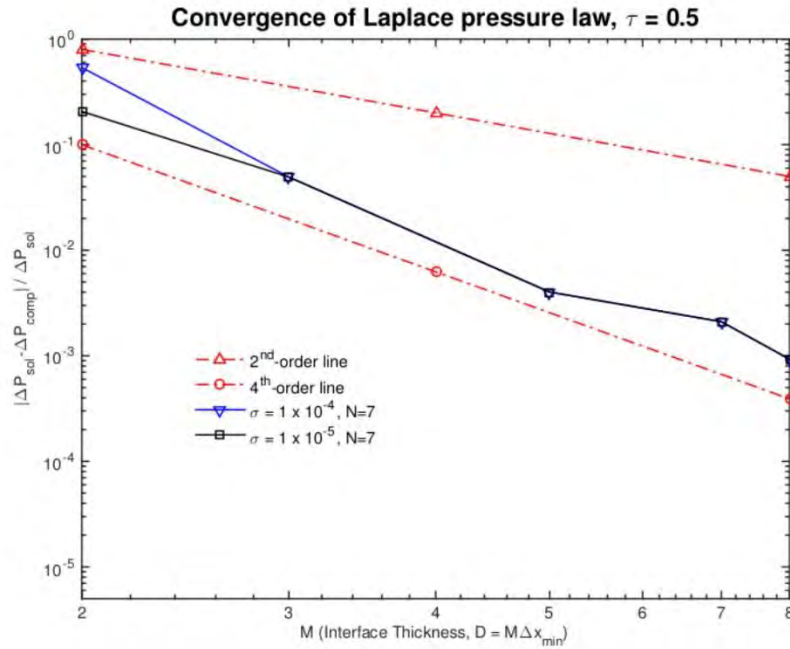


Figure 27: Convergence of Laplace law

In order to take further advantage of the body-fitting, spectral element nature of our scheme, we conduct similar 2D droplet tests on a variety of unstructured mesh distributions. The first mesh we consider is a perturbation to the simple 2D box mesh. Figure below portrays the kind of mesh we consider. This perturbation is introduced via a simple “zig-zagged” distribution that is based on the angle, θ . The reason behind this perturbation is to observe the performance of the MFS scheme on poorly designed meshes which are too skewed to capture interfacial dynamics.

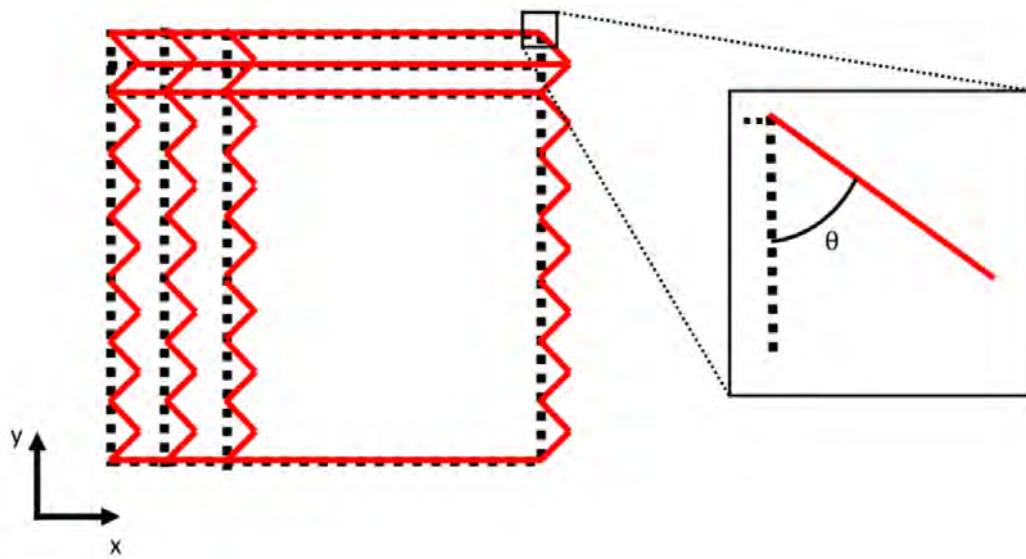


Figure 27: Zig-zagged mesh

Fig. 28 shows the time evolution of the maximum kinetic energy at different angles, θ . The measure of the perturbation is given by the coefficient $\alpha = \tan \theta$.

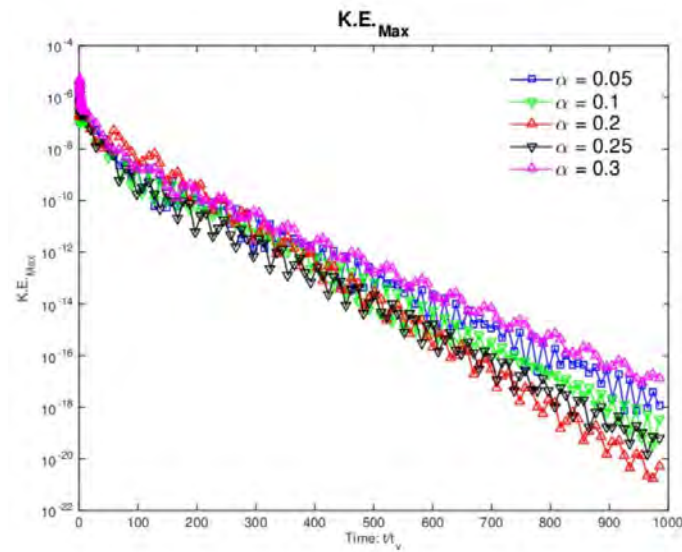


Figure 28: time evolution of the maximum kinetic energy

6. MEMS Sensor Measurement of Surface Temperature Response

Subcooled flow boiling experiments have been conducted using water at atmospheric pressure in a rectangular flow channel. These experiments are conducted to obtain high-resolution data for validation of 3-D Interface Tracking Models (ITMs) and CFD models which can predict subcooled flow boiling phenomena in fuel assemblies of Pressurized Water Reactors. The data needed for model validation include turbulent liquid flow characteristics, vapor bubble nucleation, growth and departure data, and wall temperature response during subcooled flow boiling. In our previous reports, we have presented the results of air bubble injection and subcooled flow boiling experiments conducted in an annular flow channel. In the present work, the temperature response of a MEMS sensor imbedded in the heater surface is being obtained during subcooled flow boiling of water flowing upward through a vertical rectangular test section at atmospheric pressure as shown in Fig. 29.

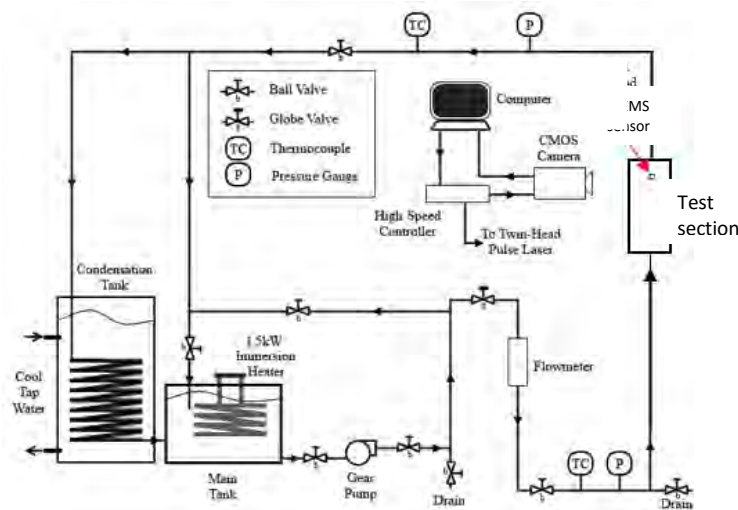


Figure 29: Subcooled Flow Boiling Loop

The rectangular flow channel is 130.0 mm long, 20.0 mm wide and 4.0 mm high. A special MEMS sensor has been developed as shown in Fig. 30 to measure the response of the heated surface temperature before, during and after the nucleation, growth and departure of a single vapor bubble. The vapor bubble nucleation is triggered by an electric pulse sent to electrodes that causes electrolysis of water and generation of a hydrogen bubble that acts as the vapor bubble nucleus. The MEMS sensor is installed on the heated surface of the rectangular test section at a location 100.0 mm downstream of the channel inlet, after an 80.0 mm long pre-heater section.

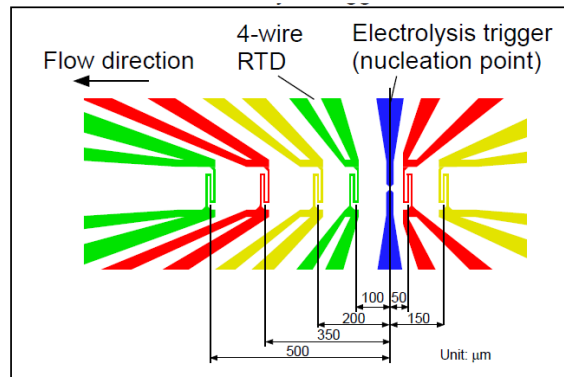


Figure 30: RTD layout in a MEMS

Sample signals from the MEMS sensor at a heat flux of 83 kW/m^2 and liquid subcooling of 10°C are shown in Fig. 31.

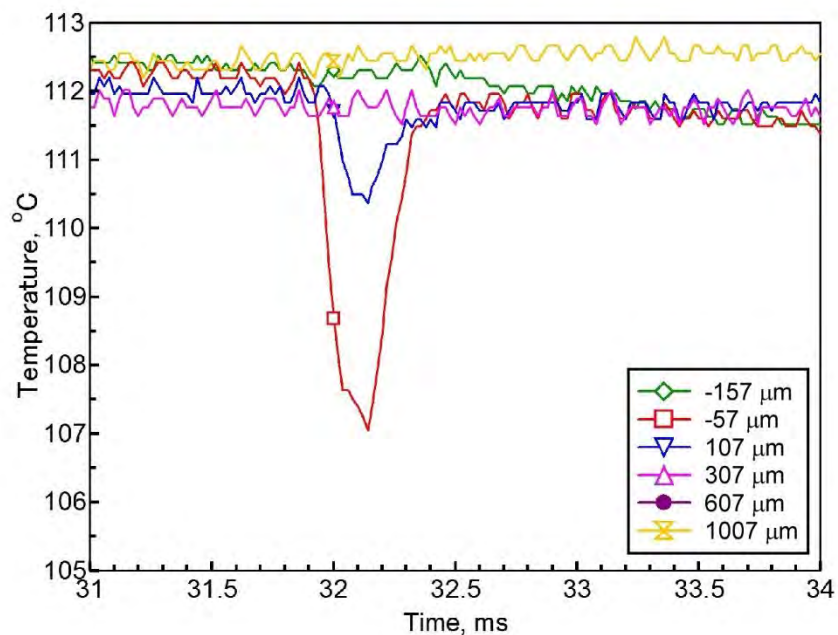


Figure 31: Output signals from a MEMS sensor

As a bubble is triggered to nucleate at 31.9 ms, the surface temperature drops rapidly and recovers within $400 \mu\text{s}$. The magnitude of the temperature drop at $57 \mu\text{m}$ from the bubble nucleation point is seen to be 5°C , and the temperature drop decreases with the distance from the bubble nucleation point as expected. At more than $150 \mu\text{m}$, there is no influence of the bubble nucleation seen for this particular bubble nucleation.

The MEMS sensor signals obtained at other times between 20 and 90 ms during the same experimental run as in Fig. 31 are shown in Figs. 32-34.

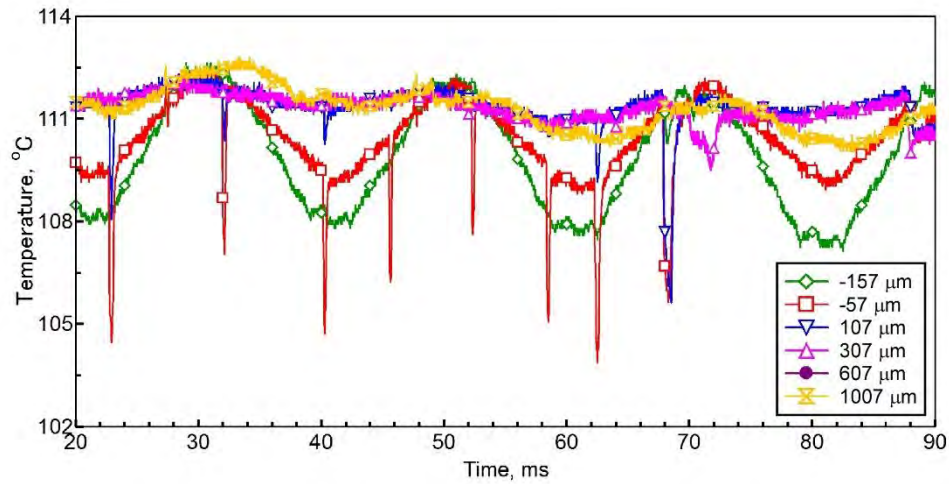


Figure 32: MEMS sensor signals for time between 20 and 90 ms

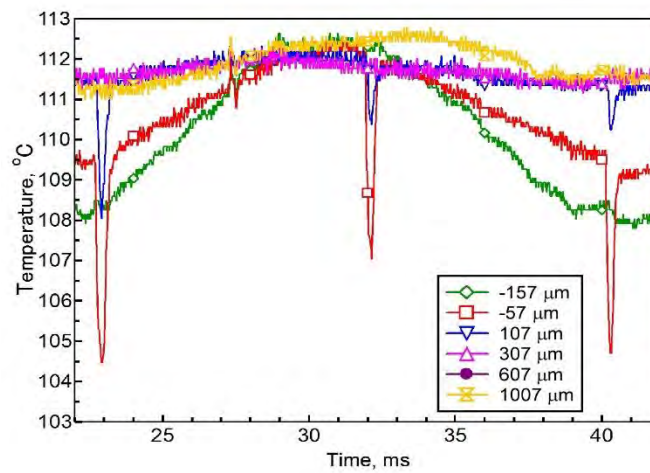


Figure 33: MEMS sensor signals for time between 20 and 90 ms

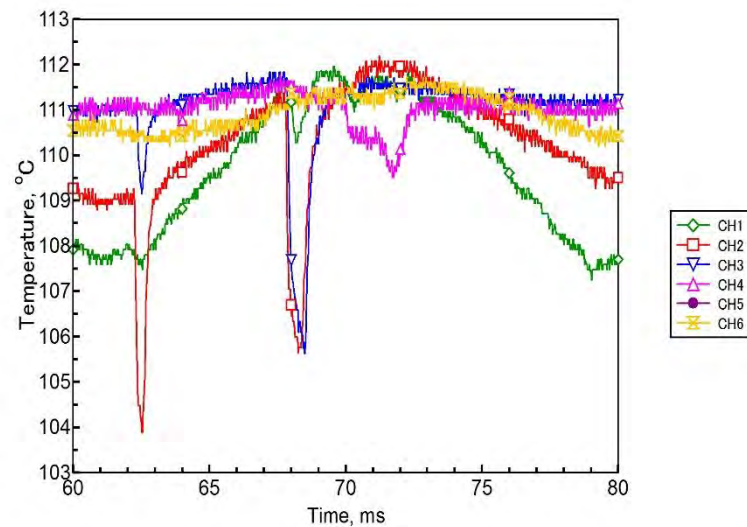


Figure 34: MEMS sensor signals for time between 60 and 80 ms

Video images of the sensor surface were also taken at a frame rate of 5,000 fps before and after bubble nucleation at the triggering point as shown in Fig. 35.

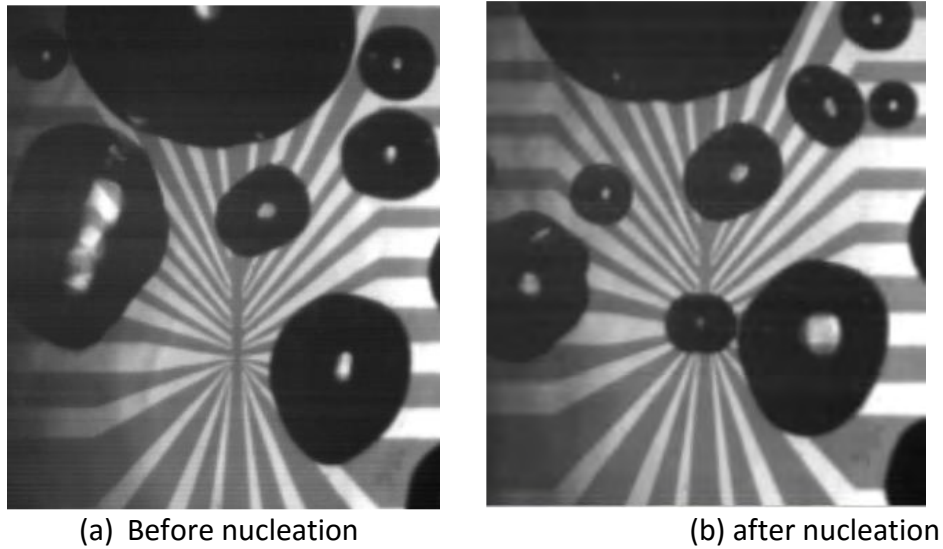


Figure 35: Video pictures of the vapor bubbles nucleating on the MEMS sensor surface at the trigger point

A digital high-speed video imaging system is also being used to capture the bubble images from the side of the rectangular flow channel, in combination with the liquid velocity profile and turbulence fluctuation measurements using a Particle-Image Tracking Velocimetry system (LaVision FlowMaster 2-D PIV System with 10 μm diameter seed particles).